Tectonics

RESEARCH ARTICLE

10.1029/2020TC006416

Key Points:

- Fault blocks of the Shanxi Rift have experienced <~2 km of footwall uplift since the Miocene
- Low-temperature thermochronometric data record region-wide cooling events at ca. 110–70 Ma and 50–30 M, prior to development of the modern Shanxi Rift
- Exhumation at ca. 50–30 Ma is coeval with the formation of the Bohai and Weihe basins during a period of regional NW-SE extension

Supporting Information:

- Supporting Information S1
- Data Set S1
- Data Set S2
- Data Set S3

Correspondence to:

C. Clinkscales,
clinkscales@email.arizona.edu

Citation:

Clinkscales, C., Kapp, P., Thomson, S., Wang, H., Laskowski, A., Orme, D. A., & Pullen, A. (2021). Regional exhumation and tectonic history of the Shanxi Rift and Taihangshan, North China. *Tectonics*, *40*, e2020TC006416. https://doi.org/10.1029/2020TC006416

Received 20 JUL 2020
Accepted 21 DEC 2020

Regional Exhumation and Tectonic History of the Shanxi Rift and Taihangshan, North China

Christopher Clinkscales[1], Paul Kapp[1], Stuart Thomson[1], Houqi Wang[2], Andrew Laskowski[3], Devon A. Orme[3], and Alex Pullen[4]

[1]Department of Geosciences, University of Arizona, Tucson, AZ, USA, [2]Center for Excellence in Tibetan Plateau Earth Sciences, Key Laboratory of Continental Collision and Plateau Uplift, Institute of Tibetan Plateau Research, Chinese Academy of Sciences, Beijing, China, [3]Department of Earth Sciences, Montana State University, Bozeman, MT, USA, [4]Department of Environment, Engineering, and Earth Sciences, Clemson University, Clemson, SC, USA

Abstract This study presents a comprehensive low-temperature thermochronometric data set from the Shanxi Rift, Taihangshan, and eastern Ordos block in North China, including new apatite fission track and apatite (U-Th-Sm)/He data and published apatite and zircon fission track and (U-Th-Sm)/He data. We use these data and new thermal history inversion models to reveal that the Shanxi Rift and Taihangshan experienced an increase in cooling rates between ca. 110–70 Ma and ca. 50–30 Ma. A preceding ca. 160–135 Ma cooling event is generally restricted to the western rift margin in the Lüliangshan and Hengshan. In contrast, the ca. 50–30 Ma cooling event was widespread and occurred coevally with the opening of the Bohai Basin and slip across the NNE-striking Eastern Taihangshan fault. In the southern rift zone, however, exhumation beginning ca. 50 Ma was likely associated with fault block uplift across the ESE–striking Qinling and Huashan faults, which accompanied the extensional opening of the Weihe Graben. Coeval fault slip along the NNE–striking Eastern Taihangshan faults and ESE–striking Qinling and Huashan faults was associated with NW-SE extension in North China related to oblique subduction of the Pacific plate under Eastern Asia and slow convergence rates. The Shanxi Rift is commonly attributed to Late Miocene and younger extension, but our new thermochronologic data do not precisely record the onset of rifting. However, our inversion models do suggest ≤~50°C of Neogene–Quaternary cooling, consistent with ≤~2 km of footwall uplift across most range-bounding faults.

1. Introduction

The Cenozoic structural geology of Asia comprises a continental-scale region of interacting strike-slip, thrust, and extensional faults (Figure 1a and 1b; e.g., Tapponnier & Molnar, 1977; Taylor & Yin, 2009). Cenozoic faulting is largely dictated by the India-Asia continental collision, the gravitational spreading of the Tibetan Plateau, and subduction along the eastern margin of Eurasia (e.g., A. Yin, 2010). In the circum-Ordos region of North China, more than 2,000 km from the nearest active plate boundary, Cenozoic deformation has produced intracontinental rifts that define the periphery of the Ordos block (Figure 1c). Along the eastern margin of the Ordos block is the ~1,000 km long late Miocene–Quaternary Shanxi Rift characterized by NE-SW—striking basins and uplifts linked by ~ N-S—striking accommodation zones (e.g., X. Xu & Ma, 1992) (Figure 2). Rifting is attributed to NW-SE extension associated with the propagation of left-lateral strike-slip faults emanating from the northern Tibetan Plateau (e.g., Peltzer et al., 1985; Tapponnier & Molnar, 1977), and the timing and mode of extension appears similar to other late Miocene and younger rift systems in the southern Himalayan-Tibetan orogen and the interior of Asia (e.g., Baikal Rift; A. Yin, 2000) (Figure 1a). The left-stepping en-echelon and sigmoid-shaped geometry of the Shanxi Rift suggests a transtensional origin, which is broadly attributed to the counterclockwise rotation of the Ordos block relative to the adjacent Alxa block and North China Plain (e.g., Middleton et al., 2016; X. Xu et al., 1993; X. Xu & Ma, 1992; Y. Q. Zhang et al., 1998; Y. Zhang et al., 2003) (Figure 1c).

In this study, we attempt to resolve the low temperature (<~120°C) cooling history of the Shanxi Rift by applying the apatite fission track (AFT) and apatite U-Th-Sm/He (AHe) thermochronometric systems, which record cooling within the upper ~4–5 km of the crust for geothermal gradients of 25–30°C/km (e.g., Reiners & Brandon, 2006). A previous study addressing the magnitude of fault footwall uplift for two fault blocks in the northern rift revealed that extension has been insufficient to exhume fully reset AFT and AHe samples

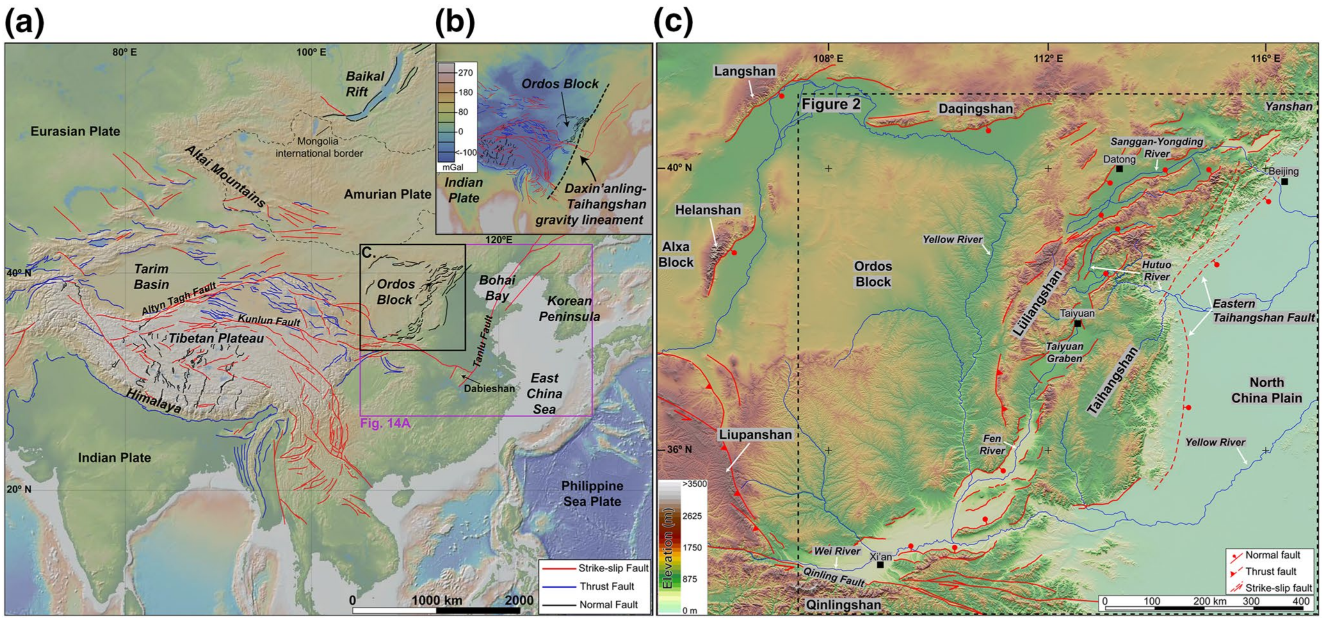

Figure 1. a) Regional fault map of central and eastern Asia. Base Global Multi-Resolution Topography map from http://www.geomapapp.org and Ryan et al. (2009). Faults in the Tibetan Plateau and surrounding regions after Styron et al. (2010). (b) Map area from (a) showing the Bouguer gravity anomalies after Bonvalot et al. (2012). (c) Digital elevation and fault map of the circum-Ordos region.

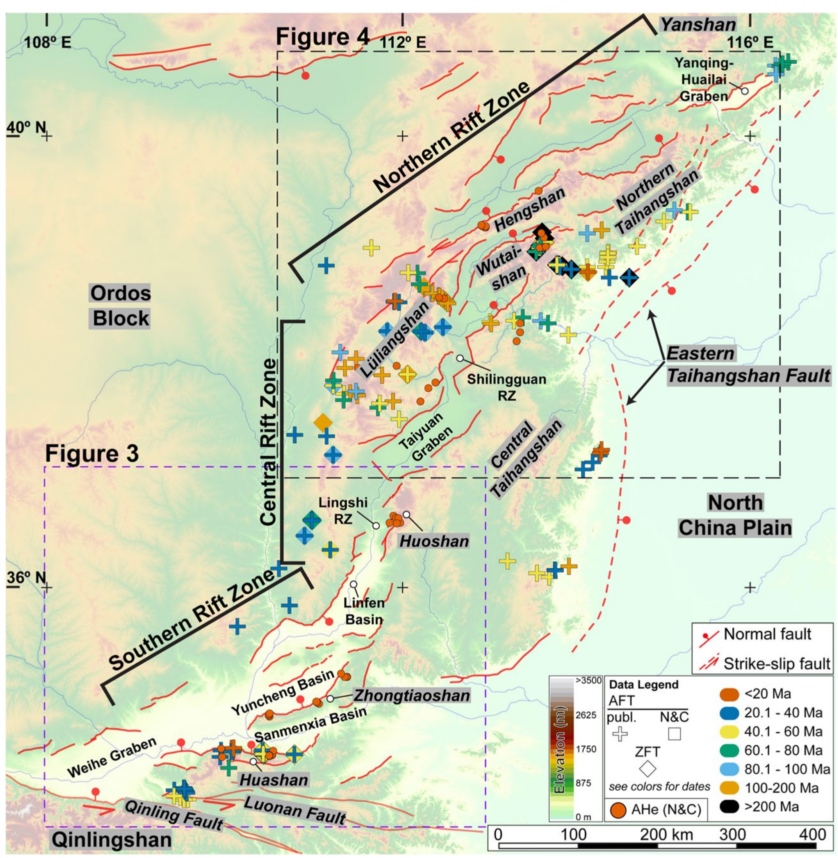

Figure 2. Map of the Shanxi Rift, Taihangshan, and eastern Ordos block showing principal range-bounding faults and locations of published and new AFT data discussed in the text. Areas of Figures 3 and 4 shown with dashed boxes. References and additional information for published (publ.) thermochronologic data are provided in the supporting information. N&C includes new data from this study and published data from Clinkscales et al. (2020). Crosses and boxes refer to AFT data; circles are AHe data; and diamonds are zircon fission track (ZFT) data. AFT, apatite fission track; AHe, apatite U-Th-Sm/He.

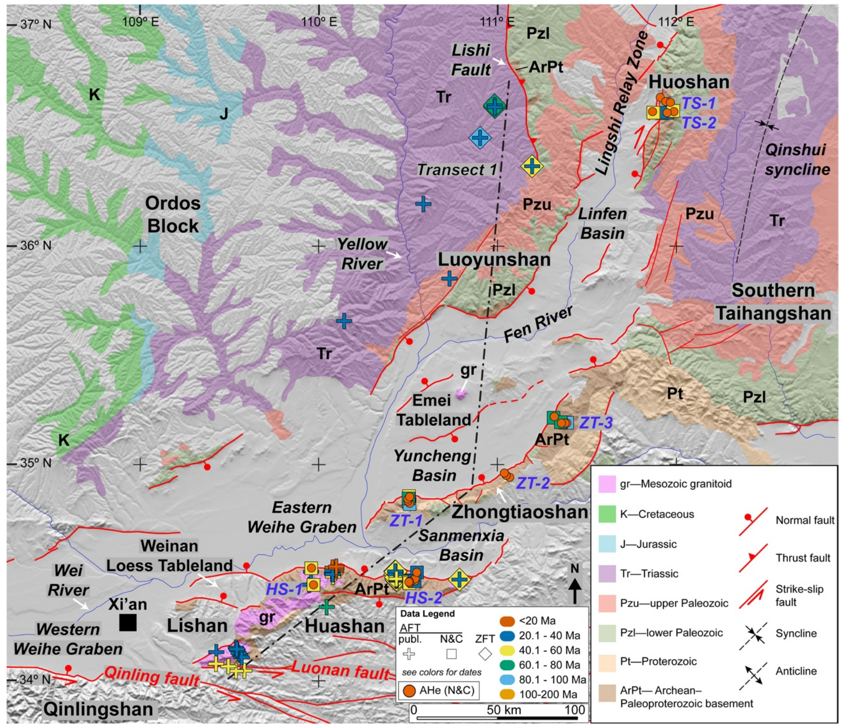

Figure 3. Bedrock geologic map of the southern and south-central Shanxi Rift. Geologic map modified after SBGMR (1989), BGMRSNX (1990), and CAGS (2002). Neogene and younger rocks are not shown. Interpretation of the Lishi Fault (west of the Lingshi relay zone) as a thrust fault after J. Zhang et al. (2020). The principal range-bounding faults are named after the associated range. References and additional information for published thermochronologic data are provided in the supporting information. N&C includes new data from this study and published data from Clinkscales et al. (2020).

yielding Neogene dates to the surface (Clinkscales et al., 2020), suggesting there has been <~2–2.5 km of footwall uplift. It is unclear, however, if the magnitude of fault footwall uplift estimated in the northern Shanxi Rift is consistent across the whole rift zone or if the low-temperature thermochronometric record is largely dictated by exhumation events which preceded the most recent rifting event. We present new AFT and AHe data and a compilation of previously published low-temperature thermochronologic data from the Shanxi Rift and neighboring Taihangshan and eastern Ordos block (Figure 2) to address: (1) the magnitude and timing of exhumation events during the Mesozoic-Cenozoic, (2) the relationship between these exhumation events to the regional tectonics of eastern Asia; and lastly, (3) estimate the maximum magnitude of Late Miocene and younger extensional exhumation across the rift. These data highlight a history of Cretaceous and Paleogene exhumation events in the structural and geomorphic evolution of North China and add additional insight into regional exhumation patterns related to slip initiation and/or reactivation across major fault systems in North China.

2. Geologic Background

2.1. Regional Framework

The Shanxi Rift is an intracontinental rift system in North China located between the Ordos block to the west and the Taihangshan and North China Plain to the east. The eastern margin of the rift zone is defined by the Taihangshan ("shan" = mountains), a broad (~60–200 km wide) range bounded to the east by the Eastern Taihangshan fault, which divides the Taihangshan from the low-lying North China Plain. The southern boundary is delimited by the left-lateral Qinling and Luonan faults (Figure 2).

The Taihangshan and Eastern Taihangshan fault coincide with the ~NNE-SSW Daxin'anling-Taihangshan gravity lineament which traverses >3,500 km across South to Northeast China and represents a divide be-

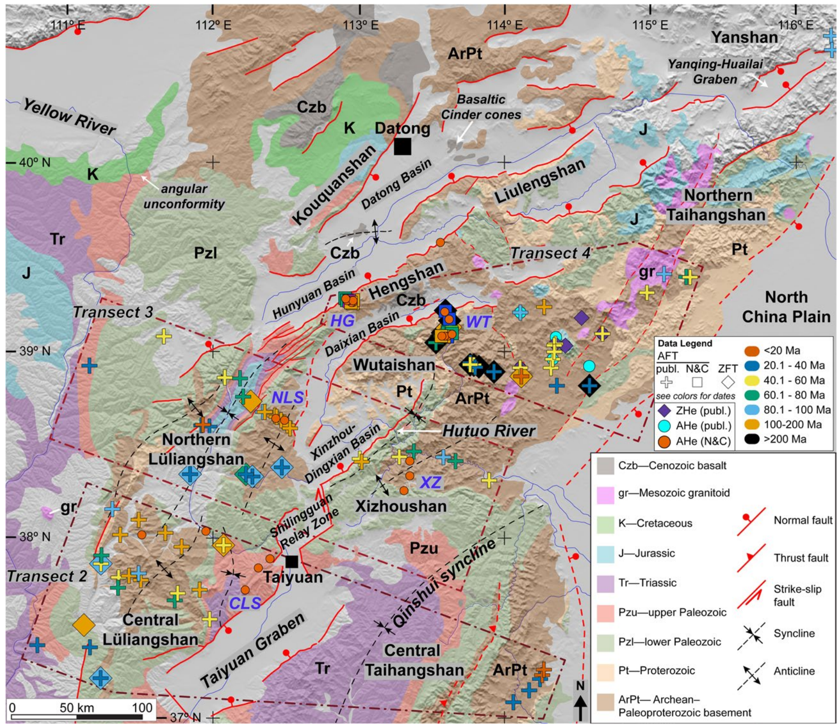

Figure 4. Bedrock geologic map of the central and northern Shanxi Rift. Geologic map modified after SBGMR (1989) and HBGMR (1989). Neogene and younger rocks are not shown except for labeled basaltic rocks. The principal range-bounding faults are named after the associated range. References and additional information for published thermochronologic data are provided in the supporting information. N&C includes new data from this study and published data from Clinkscales et al. (2020).

tween negative Bouguer gravity anomaly values (<−50 mGal) to the west and weakly negative to positive gravity anomaly values (−25 to >25 mGal) to the east (Figure 1b; Y. G. Xu, 2007). This gravity lineament is also referred to as the "Great Gradient Line" (e.g., Guo et al., 2020) and its location coincides with a significant change in the thickness of the lithosphere from <100 km under the North China Plain and Bohai Bay to ~140–160 km (Y. Li et al., 2013; Z. Zhang et al., 2014) or >200 km (Priestley et al., 2006) under the Ordos block. An increase in the crustal thickness is also observed at the eastern Taihangshan, from ~30 to 35 km under the North China Plain and Bohai Bay to ~45 km under the Ordos block (Tian et al., 2014; Xia et al., 2017). This increase in crustal thickness inversely correlates with average heat flow gradients, decreasing from 32°C/km ± 5°C/km in Bohai Bay (Qiu et al., 2010) to ~26°C/km in the Shanxi Rift (X. Xu et al., 1993).

The Taihangshan and Shanxi Rift overlap with a former NNE-striking Late Archean-Paleoproterozoic orogenic belt, referred to as the Trans-North China Orogen or Central Orogenic Belt (e.g., Kusky et al., 2007). This orogenic belt defines the boundary between the western and eastern blocks of the North China Craton. The Eastern Taihangshan fault has been interpreted as a Proterozoic suture that closed during amalgamation of these two blocks (Faure et al., 2007), thus, the change in the lithospheric and crustal architecture of North China at the Eastern Taihangshan fault and neighboring Taihangshan may coincide with the location of antecedent Paleoproterozoic structures (e.g., Z. Zhang, Teng, et al., 2014). The basement rocks of the Taihangshan and Shanxi Rift dominantly consist of ca. 2500 Ga orthogneisses, granitoids, and metavolcanic rocks that underwent high-grade metamorphism at ca. 1.85 Ga (e.g., Kröner et al., 2005; Trap et al., 2009, 2007). Basement rocks are nonconformably overlain by Proterozoic sedimentary and meta-sedimentary rocks and Paleozoic strata (SBGMR, 1989). The lower Paleozoic section consists of Cambrian to Ordovician siliciclastic and carbonate strata (Meng et al., 1997), which is bounded at its top by a regional unconformity separating the overlying upper Paleozoic section. The upper Paleozoic consists of Carboniferous to Permian strata which vertically grade from a marine to non-marine, siliciclastic-dominated section, overlain by a Mesozoic section consisting of Triassic-Lower Cretaceous non-marine sedimentary and volcanic strata (e.g., SBGMR, 1989; H. Xu et al., 2019). Early Cretaceous igneous rocks crop out across the region and are typically in the age range of ca. 140–130 Ma (Figures 3 and 4; e.g., J. Hu et al., 2012; S. H. Zhang, Zhao, et al., 2014).

2.2. Geology of the Shanxi Rift

The Shanxi Rift is divided into three main segments: (1) the southern segment, located between the Huashan to the south, north of the Luonan and Qinling faults, and the Linfen Basin to the north; (2) the central segment, centered on the Taiyuan graben and bounded to its southwest and northeast, respectively, by the Lingshi and Shilingguan relay (accommodation) zones; and (3) the northern segment, from the northern Lüliangshan and Wutaishan to the Yanqing-Huailai graben and Yanshan to the north (Figure 2). This subdivision differs slightly from previous workers (e.g., X. Xu & Ma, 1992) in that the Huashan, eastern Weihe Graben, and Sanmenxia Basin are included within the southernmost Shanxi Rift. The three segments together comprise a sigmoid-shaped rift system. For reference, range-bounding faults are commonly named after their adjacent range (e.g., Shi et al., 2015, 2020).

2.2.1. Southern Rift

The principal uplifts in the southern segment include the Huashan, Zhongtiaoshan, and Luoyunshan, and the subsidiary Lishan, Weinan, and Emei Tableland fault blocks (Figure 3). The Huashan is defined along its western margin by a series of left-stepping en-echelon normal faults and is delimited to the south by the left-lateral Luonan fault (e.g., A. Zhang et al., 1995). The northern Huashan is an ~ E-W-striking footwall block bounded by the Huashan fault to the north (i.e., Taiyao fault; e.g., Y.-T. Wang et al., 2019) and a S-dipping fault to the southeast (Figure 3). The Huashan fault juxtaposes Neogene-Quaternary strata in its hanging wall against Neoarchean-Paleoproterozoic basement rocks (e.g., X. Yu, Liu, Li, et al., 2013) and ca. 200 Ma and ca. 140–130 Ma Mesozoic granitoids in its footwall (e.g., H. Chen et al., 2015; J. Hu et al., 2012).

West of the Huashan is the Weinan Loess Tableland and the Lishan. The Lishan is a subsidiary fault block that exposes Neoarchean basement rocks unconformably overlain by Eocene-Neogene strata (BGMRSNX, 1990). This Eocene and younger section is likely correlative to the buried Cenozoic sedimentary rocks of the Weihe Graben (e.g., Lu et al., 2019) and attests to the fault block segmentation of the Weihe Basin after the Oligocene. The Weinan Tableland is draped by Quaternary loess deposits.

The Zhongtiaoshan, north of the Sanmenxia Basin, is an asymmetric horst block in the footwall of the Zhongtiaoshan fault. The Zhongtiaoshan fault, along the northern margin of the range, juxtaposes basement rocks against Neogene-Quaternary deposits of the Yuncheng Basin. Neoarchean-Paleoproterozoic basement rocks crop out along its northern escarpment and are unconformably overlain by south-dipping Proterozoic-Paleozoic strata (BGMRSNX, 1990).

The basins of the southern segment include the interconnected Weihe, Sanmenxia, Yuncheng, and Linfen basins (Figure 3). The Weihe graben is subdivided into a western and eastern segment (e.g., Qu et al., 2018; A. Zhang et al., 1995). Its western segment is defined by the Qinling fault to the south and the eastern segment is delimited to the south by the range-bounding faults of the Lishan, Weinan Loess Tableland, and Huashan. The Weihe Graben is at a surface elevation of ~350–500 m and is infilled with ~5,000–7,000 m of Eocene-Quaternary strata (J. M. Wang, 1987; Y. Q. Zhang et al., 1998). The Sanmenxia Basin to the east in infilled with a correlative Eocene-Quaternary section that is < 2,000 m thick (Shi et al., 2019, their Figure 3). In comparison, the Yuncheng Basin north of the Zhongtiaoshan is infilled with as much as ~5,000 m of Miocene (ca. 7 Ma) and younger strata (Q. Wang et al., 2002) and is an asymmetric graben with its thickest accumulation to the southeast adjacent to the Zhongtiaoshan fault (e.g., Shi et al., 2020). To the northeast, the Zhongtiaoshan fault and Yuncheng Basin exhibit a change in strike orientation from ENE (~070–080°) to NNE (~30–35°) into the Linfen Basin. The Linfen Basin is infilled with upper Miocene-Pliocene and younger strata which thickens to the northwest to ~1,800–2,200 m toward the Luoyunshan fault (Shi et al., 2020; X. Xu & Ma, 1992).

2.2.2. Central Rift

The principal uplifts in the central rift are the Huoshan, central Lüliangshan, and Xizhoushan (Figure 2). The southern boundary of the central rift zone is at the ~NNE-SSW-striking Lingshi relay zone (also referred to as the Lingshi "push-up swell"), bounded to the east by the Huoshan fault (e.g., Shi et al., 2015; X. Xu et al., 1993) (Figures 2 and 3). The southern segment of the Lingshi relay zone is defined by the northern Linfen Basin, which is infilled with as much as ~1,600 m of Pliocene-Quaternary sediment. In comparison, the central segment of the Lingshi relay zone is characterized by < 1,000 m of Pliocene-Quaternary strata (X. Xu & Ma, 1992).

The Huoshan is an east-dipping fault block bordered to the west by left-stepping en-echelon fault segments of the frontal Huoshan fault system. Within the range, Archean-Paleoproterozoic rocks are exposed to the west and unconformably overlain by ESE-dipping Paleozoic-Triassic sedimentary rocks (Figure 3). This E-dipping panel comprises the western limb of the Qinshui syncline, which is one of several Late Jurassic-earliest Cretaceous basement-involved folds located in the Taihangshan and central Shanxi Rift (Clinkscales & Kapp, 2019; J. Zhang et al., 2020; H. Zhao et al., 2020). At the northern margin of the Huoshan, lower Paleozoic-Triassic strata are faulted against Neogene-Quaternary sediment of the Taiyuan Graben (Figures 3 and 4). Trench studies suggest the Huoshan fault is characterized by latest dip-slip offset (Y. Xu et al., 2018), although previous studies indicate a right-lateral sense of displacement from offset gullies (e.g., Y. Q. Zhang et al., 1998).

To the north of the Huoshan fault is the NE-SW-striking Taiyuan graben, bounded by conjugate SE- and NW-dipping normal faults (X. Xu & Ma, 1992). The surface of the basin is at an elevation of ~700–800 m, >200 m higher than the surface of the Weihe graben. The Taiyuan graben is asymmetric with a ~3,800 m thick Pliocene-Quaternary syn-rift sedimentary section along the northwestern margin of the basin bordering the Lüliangshan, which thins to the southeast to <1,000 m (X. Xu et al., 1993).

The Lüliangshan is separated from the Taiyuan Graben by a SE-dipping normal fault (Figure 4). Lower Paleozoic-Triassic strata are faulted against the Neogene-Quaternary strata of the Taiyuan Graben and are folded as part of a NNE-SSW–trending syncline. Neoarchean-Paleoproterozoic basement rocks in the Lüliangshan represent the cores of basement-involved anticlines and Triassic-Jurassic strata are preserved in the cores of synclines (Clinkscales & Kapp, 2019; H. Zhao et al., 2020).

The northern Taiyuan graben terminates against the ~NNE-SSW-striking Shilingguan relay zone (i.e., Shilingguan "push-up swell"; X. Xu et al., 1993) (Figures 2 and 4). The Shilingguan relay zone differs from the Linghsi in that it is defined by NNW–striking (~340–345°) range-bounding faults along its western and eastern margins. These faults are nearly orthogonal to the principal NE-SW-range-bounding faults and likely represent extensional-parallel faults formed within an antithetic transfer zone (e.g., Faulds & Varga, 1998). North of the Shilingguan relay zone is the Xinzhou-Dingxiang Basin, an asymmetric half-graben at a surface elevation of ~750–800 m, which is infilled with as much as ~1,800 m of syn-rift sedimentary rocks and bounded by the Xizhoushan fault (e.g., X. Xu & Ma, 1992) (Figure 4).

The Xizhoushan is characterized by folded Archean-Paleoproterozoic basement rocks and lower-upper Paleozoic strata (Clinkscales & Kapp, 2019; SBGMR, 1989). The northwestern escarpment of the range is characterized by Neoarchean-Paleoproterozoic basement rocks, Paleoproterozoic metasedimentary rocks, and lower Paleozoic strata that comprise the northwestern limb of the Xizhou syncline and are faulted against Neogene-Quaternary strata of the Xinzhou-Dingxiang Basin (Figure 4).

2.2.3. Northern Rift

The northern Shanxi Rift extends from the northern Lüliangshan and Wutaishan to the Yanshan (Figures 2 and 4). The ranges that will be discussed in this study include the Wutaishan, northern Lüliangshan, and Hengshan. To the north of these ranges, the principal fault blocks are the Kouquanshan, Liulengshan, and the northern Taihangshan (Figure 4). Neotectonic studies indicate that the northern Shanxi Rift is horizontally extending at ~1–2 mm/a at an azimuth of ~151° (Middleton et al., 2017).

The Wutaishan and Hengshan are southeast-tilted footwall blocks separated by the Daixian Basin (Figure 4). The Daixian Basin parallels the NE-SW-striking Wutaishan fault, is ~10 km wide, and is infilled with ~1800 m of Pliocene and younger sediment near the Wutaishan fault (e.g., X. Xu & Ma, 1992). To the southwest, between the Wutaishan and Lüliangshan, the orientation of the Daixian Basin shifts to a NNE-SSW (~010°) direction. This orientation is similar to the NNE-striking Huoshan fault and Lingshi relay zone of the central segment, which suggests that the southwestern Daixian Basin and eastern margin of the Lüliangshan likely represents a relay zone between the Wutaishan fault and the Xinzhou-Dingxiang Basin.

The Wutaishan, Hengshan, and northern Lüliangshan expose Archean-Paleoproterozoic basement rocks unconformably overlain by Paleoproterozoic metasedimentary and lower Paleozoic strata (Figure 4). The Archean-Paleoproterozoic basement is dominated by tonalite-trondhjemite-granodiorite orthogneisses, migmatites, and granitoid intrusions. In the Wutaishan, the basement rocks are part of the Wutai complex, which includes abundant amphibolites, paragneisses, and "greenstone belt" rocks, including metavolcanics rocks (e.g., Kröner et al., 2005). These basement rocks are principally overlain by metasedimentary rocks of the Hutou Group (e.g., S. Li et al., 2010). This unconformable relationship varies through the region, and elsewhere (e.g., Hengshan, Lüliangshan, and southwest Xizhoushan), basement rocks are unconformably overlain by lower Paleozoic strata (SBGMR, 1989). The southern Wutaishan is dominated by Hutuo Group rocks which presumably comprise the northwestern limb of the Xizhou syncline (Figure 4). In the northern Lüliangshan, basement and lower Paleozoic to Jurassic strata were folded during an episode of Late Jurassic–Early Cretaceous northwest-southeast shortening, known as the Yanshanian orogenic event of North China (e.g., Clinkscales & Kapp, 2019; Y. Zhang et al., 2008).

Oligocene–Quaternary basalts crop out in the northern Shanxi Rift (Figure 4), unlike the southern and central segments which were largely amagmatic during the Cenozoic. Along the southeastern margin of the Hengshan, Oligocene basalts are gently back-tilted to the southeast (SBGMR, 1989). These basalts were erupted between ca. 26–24 Ma and their geochemistry is consistent with melts originating from partially melted asthenosphere with a mixed contribution from the Archean-Paleoproterozoic mantle lithosphere of the North China Craton (Tang et al., 2006). An outcrop of basalts located between the Hunyuan and Datong basins are likely correlative to the Oligocene basalts in the Hengshan (Figure 3; e.g., Shi et al., 2020). Basaltic flows interbedded with lacustrine and fluvial strata in the northern Kouquanshan range in age from ca. 22 to 10 Ma (S. Chen et al., 2001; S. Li et al., 1988) or ca. 27–14 Ma (e.g., Y. Hu et al., 2016 and reference therein). Younger late Miocene (ca. 8 Ma) basalt flows are also offset by the northern strand of the Kouquanshan fault (Middleton et al., 2017). In the Datong Basin, Pleistocene cinder cones crop out and their coeval, flanking basalts flows are interbedded with lacustrine and loess deposits (Figure 4; X. Xu et al., 1993; Y. Li et al., 1998).

2.2.4. Planation Surfaces

The footwall blocks of the Shanxi Rift reveal three prominent planation, or low-relief, bedrock-floored surfaces interpreted to have developed during intermittent periods of tectonic and/or climatic stability (e.g., Xiong et al., 2018). These planation surfaces are the Late Cretaceous-early Eocene Beitai, late Oligocene Dianziliang, and late Miocene-Pliocene Tangxian surfaces, and their timing of development, although disputed, is constrained by ages of overlying regolith, red clay, loess, conglomeratic deposits, or basalt flows (e.g., K. Zhang, 2008; Xiong et al., 2018, 2017). Low-temperature thermochronologic studies have also suggested that these planation surfaces coincided with cooling events during the Cretaceous and Paleogene (Cao et al., 2015; Chang et al., 2019; S. B. Li et al., 2015; Qing et al., 2008). The major planation surfaces, from oldest to youngest, include: the Beitai surface at elevations of ~2,500–3,050 m, including the summit of Wutaishan and the western Lüliangshan; the medial Dianziliang surface located at elevations of ~1,500–2,100 m, including the ridgeline of the Hengshan and eastern Lüliangshan; and the lower Tangxian surface at elevations of ~400–1,400 m, which includes piedmont surfaces near the frontal escarpments of the uplifted footwall blocks and along the margin of the Ordos block, and at elevations of ~50–600 m in the eastern Taihangshan near the North China Plain (Figure 2; Xiong et al., 2018 and references therein). The Tangxian surface is dated to at least ca. 3.1 Ma from magnetostratigraphic studies of the overlying sedimentary rocks in the Zhongtiaoshan (Xiong et al., 2018), which are likely correlative to uplifted ca. 3 Ma terrace deposits in the northern Shanxi Rift (Deng et al., 2008; Xiong et al., 2017).

2.3. Eastern Ordos Block (Basin)

Located west of the Shanxi Rift is the Ordos block (Figure 1). The Ordos block represents a region of thick crust, up to ~40–45 km (e.g., Tian et al., 2014), with Cenozoic deformation localized along its periphery (e.g., Y. Zhang et al., 2003). The periphery of the block may be a long-lived mechanical boundary that dates back to the Middle Jurassic-Early Cretaceous Yanshanian orogeny or earlier (e.g., Darby & Ritts, 2002). The Ordos block coincides with the location of the former intracontinental Ordos Basin, which experienced its latest phase of subsidence during the Middle Jurassic–Early Cretaceous Yanshanian orogeny (e.g., Ritts et al., 2009). In the eastern Ordos block, along the margin of the Shanxi Rift, Paleozoic–Cretaceous strata dip shallowly to the west and generally crop out in incised river valleys (Figures 3 and 4). In the northern Ordos, Lower Cretaceous rocks rest in angular unconformity over the pre-Cretaceous strata and basement rocks (Figure 4). The Paleozoic-Mesozoic strata are unconformably overlain by upper Miocene-Pliocene (ca. 8–5 Ma) and/or younger loess-paleosol deposits of the Chinese Loess Plateau (e.g., Nie et al., 2016).

3. Methods

We present new AFT ($N = 22$) and AHe ($N = 37$ (number of samples); $n = 142$ (single-grain analyses)) from the Huashan, Zhongtiaoshan, Huoshan, Lüliangshan, and Taihangshan. Samples were primarily collected from Archean–Paleoproterozoic basement rocks; the exception are four samples (single-grain analyses, $n = 15$) from the Lüliangshan and Taihangshan from lower and upper Paleozoic and Triassic sandstones. Sample information shown in Table 1.

3.1. Apatite Fission Track

The AFT method is based on the temperature- and time-dependent annealing of fission tracks produced by the spontaneous decay of ^{238}U in an apatite crystal (e.g., Donelick et al., 2005). The AFT method is useful in discerning the time-temperature (t-T) history of a sample through the temperatures of ~120–60°C, a temperature range referred to as the partial annealing zone (PAZ; e.g., Fitzgerald & Malusà, 2019). At temperatures > ~120°C (i.e., below the PAZ), fission tracks effectively anneal spontaneously over geologic time (i.e., >~1 m.y.). Within the PAZ, fission tracks will partially anneal, and above the PAZ, tracks will effectively remain their original length (~16–16.5 μm) with a minor reduction in length (e.g., Gleadow, Duddy, Green, & Lovering, 1986; Green, 1988). A statistically robust population of confined track length measurements combined with ~20 single-grain counts from a single sample can be used to constrain t-T histories through use of inverse thermal modeling and thus determine the approximate time a sample resided in or above the PAZ (e.g., Ketcham, 2005). AFT analyses of 22 samples were conducted at the University of Arizona Fission Track Laboratory and AFT dates were determined by applying the external detector method (Gleadow, 1981). AFT data are summarized in Table 2 and dates are reported as central dates at 1σ uncertainty. Additional details on AFT methodology are presented in the supplementary data.

3.2. Apatite (U-Th-Sm)/He

The AHe method measures the concentration of ^{4}He (alpha particles) against the parent isotopes of ^{238}U, ^{235}U, ^{232}Th, and ^{147}Sm to calculate the amount of time a grain has resided at temperatures less than its closure temperature (e.g., Farley, 2002). The "closure date" or "He cooling age" of a single apatite grain is controlled by the rate of cooling (e.g., Reiners & Brandon, 2006), and can be influenced by the time spent within the partial retention zone (PRZ), most commonly in the range of ~40–85°C (e.g., Wolf et al., 1998). The PRZ and effective closure temperature can vary based of differences in a grain's chemistry, parent nuclide zonation, size, and subjected cooling rates (e.g., Farley et al., 2011; Fitzgerald et al., 2006; Flowers et al., 2009; Shuster et al., 2006). In this study, we only test for potential date differences by comparing the single grain dates against parent nuclide content ($eU = U + 0.235 \times \mathrm{Th}$) and grain size (Rs, equivalent spherical radius). Apatite grains with higher eU values are presumed to be more retentive and characterized by higher closure temperatures, and thus typically yield older AHe dates (Shuster et al., 2006). Larger grains may also be more retentive and associated with higher closure temperatures (e.g., Farley, 2000, 2002). Departures from these simple assumptions may be indicative of additional complexities such as, the occurrence of inclusions within the grain (Vermeesch et al., 2007), helium loss, helium addition (i.e., excess helium), and/or

Table 1
Sample Names and Information

Sample name	Traverse	Elevation (m)	Latitude (°N)	Longitude (°E)	Lithology	Age	AFT data	AHe data
HS-1-390	HS-1	390	34.5189	109.9585	Gneiss	Neoarchean–Paleoproterozoic	X	X
HS-1-1840	HS-1	1840	34.4418	109.9716	Granitoid	Early Cretaceous	X	X
HS-2-590	HS-2	590	34.4993	110.5506	Gneiss	Neoarchean–Paleoproterozoic	X	X
HS-2-800	HS-2	800	34.4707	110.5360	Granitoid	Early Cretaceous	X	X
HS-2-964	HS-2	964	34.4586	110.5371	Granitoid	Early Cretaceous	X	X
HS-2-1150	HS-2	1150	34.4624	110.5150	Granitoid	Early Cretaceous	X	X
HS-2-1592	HS-2	1592	34.4584	110.5079	Granitoid	Early Cretaceous	X	X
HS-2-1810	HS-2	1810	34.4553	110.5052	Granitoid	Early Cretaceous	X	X
HS-2-2100	HS-2	2100	34.4500	110.5085	Granitoid	Early Cretaceous	X	X
ZT-1-476	ZT-1	476	34.8532	110.5066	Granitic Pegmatite	Neoarchean–Paleoproterozoic	X	X
ZT-1-750	ZT-1	750	34.8424	110.5037	Granitoid	Neoarchean–Paleoproterozoic	X	X
ZT-1-1022	ZT-1	1022	34.8321	110.5040	Granitoid	Neoarchean–Paleoproterozoic	X	X
ZT-1-1240	ZT-1	1240	34.8299	110.5037	Granitoid	Neoarchean–Paleoproterozoic	X	X
ZT-1-1560	ZT-1	1560	34.8160	110.5097	Granitoid	Neoarchean–Paleoproterozoic	X	X
ZT-2-448	ZT-2	448	34.9618	111.0359	Gneiss	Neoarchean–Paleoproterozoic		X
ZT-2-674	ZT-2	674	34.9499	111.0517	Gneiss	Neoarchean–Paleoproterozoic		X
ZT-2-930	ZT-2	930	34.9444	111.0675	Granitoid	Neoarchean–Paleoproterozoic		X
ZT-3-528	ZT-3	528	35.2152	111.3155	Gneiss	Neoarchean–Paleoproterozoic	X	X
ZT-3-806	ZT-3	806	35.1944	111.3566	Gneiss	Neoarchean–Paleoproterozoic	X	X
ZT-3-1090	ZT-3	1090	35.1925	111.3820	Gneiss	Neoarchean–Paleoproterozoic	X	X
ZT-3-1346	ZT-3	1346	35.1917	111.3915	Gneiss	Neoarchean–Paleoproterozoic	X	X
TS-1-1241	TS-1	1241	36.6742	111.9134	Gneiss	Neoarchean–Paleoproterozoic		X
TS-1-1584	TS-1	1584	36.6553	111.9440	Granitoid	Neoarchean–Paleoproterozoic		X
TS-1-2034	TS-1	2034	36.6515	111.9697	Gneiss	Neoarchean–Paleoproterozoic		X
TS-2-847	TS-2	847	36.6052	111.8741	Gneiss	Neoarchean–Paleoproterozoic	X	X
TS-2-1042	TS-2	1042	36.60415	111.92437	Granitoid	Neoarchean–Paleoproterozoic	X	
TS-2-1245	TS-2	1245	36.6050	111.9516	Gneiss	Neoarchean–Paleoproterozoic	X	X
TS-2-1456	TS-2	1456	36.6132	111.9857	Gneiss	Neoarchean–Paleoproterozoic	X	X
CLS-Sst-1311	CLS	1311	37.8770	112.3921	Sandstone	Upper Paleozoic		X
CLS-Sst-1612	CLS	1612	37.8334	112.3072	Sandstone	Upper Paleozoic		X
CLS-Sst-1376	CLS	1376	37.7100	112.2172	Sandstone	Triassic		X
CLS-BSMT-1062	CLS	1062	38.0322	111.9538	Gneiss	Neoarchean–Paleoproterozoic		X
CLS-BSMT-1720	CLS	1720	38.0073	111.5055	Granitoid	Neoarchean–Paleoproterozoic		X
NLS-BSMT-1270	NLS	1270	38.6259	112.4861	Granitic Pegmatite	Neoarchean–Paleoproterozoic		X
NLS-BSMT-1630	NLS	1630	38.6422	112.4307	Gneiss	Neoarchean–Paleoproterozoic		X
XZ-BSMT-589	XZ	589	38.4126	113.3527	Gneiss	Neoarchean–Paleoproterozoic		X
XZ-BSMT-692	XZ	692	38.3333	113.3467	Granitic Pegmatite	Neoarchean–Paleoproterozoic		X
XZ-SSt-843	XZ	843	38.2487	113.3089	Sandstone	Lower Paleozoic (Cambrian)		X

Abbreviations: AFT, apatite fission track; Ahe, apatite (U-Th-Sm)/He.

Table 2
Summary of AFT Results

Sample name	# Crystals	P(χ2) (%)	Central age (Ma)	± 1σ	# CTLs	Mean track length (um)	± 1 S.E.	TLSD (μm)
HS-1-390	20	99.9	41.3	6.8	5	14.37	0.53	1.06
HS-1-1840	20	99.8	46.3	4.5	2	14.39	0	0
HS-2-590	20	94.4	33	1.8	63	13.07	0.14	1.12
HS-2-964	20	99.7	35.8	4.4	Na	Na	na	na
HS-2-1150	20	99.8	36.3	3.2	14	13.42	0.21	0.7
HS-2-1370	20	98.6	35.4	3.1	29	14.36	0.17	0.9
HS-2-1592	20	99.9	42.4	3.1	29	14.21	0.18	0.9
HS-2-1810	20	99.9	46	3.2	39	14.21	0.15	0.9
HS-2-2100	20	99.9	46.8	3.2	21	14.58	0.23	1
ZT-1-476	20	99.8	45.1	2.6	71	13.57	0.19	1.5
ZT-1-750	20	99.9	64	3.8	42	13.37	0.25	1.5
ZT-1-1022	20	98.4	82.1	4	100	12.81	0.17	1.6
ZT-1-1240	20	99.6	94.9	4.5	100	12.71	0.18	1.7
ZT-1-1560	20	99.9	94.4	4.5	100	13.38	0.11	1.1
TS-2-847	20	99.9	43.1	2.4	47	14.41	0.17	1.1
TS-2-1042	6	89	40.1	6.3	5	14.21	0.69	1.3
TS-2-1245	20	99.4	39.9	2.7	10	13.57	0.28	0.8
TS-2-1456	15	98.3	42.4	2.1	100	14.43	0.12	1.2
ZT-3-528	20	99	72	3.5	100	13.37	0.11	1.1
ZT-3-806	20	99.9	72.3	5	56	12.77	0.27	1.97
ZT-3-1090	20	99.9	85.7	5.4	72	12.81	0.24	1.98
ZT-3-1346	20	99.9	95.7	6.9	15	13.3	0.37	1.37

Note. Pχ2: P-value of a chi-square test.
Abbreviations: AFT, apatite fission track; CTLs, confined track lengths; S.E., standard error; TLSD, track length standard deviation.

the heterogeneous distribution of parent nuclide content within a grain (e.g., Farley et al., 2011; Flowers & Kelley, 2011). Significant date dispersion, particularly for samples exhibiting a positive date-eU correlation, may indicate extended residence periods within the PRZ, versus overlapping intra-sample dates which are often produced by rapid cooling through the PRZ (e.g., Fitzgerald et al., 2006). Here we report mean AHe dates if ≥ 3 grains were used to calculate the mean date and if the 1σ standard deviation on the sample mean (i.e., 1σ sample standard deviation) is ≤~20% (e.g., Flowers & Kelley, 2011) after excluding anomalously old or young grains. Single grain AHe analyses ($n = 142$) were conducted at the Arizona Radiogenic Helium Dating Laboratory at the University of Arizona. AHe data are summarized in Table 3 and details on lab methodology are presented in the supplementary material.

3.3. Inverse Thermal History Modeling

To evaluate the thermal histories of individual samples from the Shanxi Rift, we carried out inverse thermal history modeling using HeFTy software (version 1.9.3; Ketcham, 2005; Ketcham et al., 2007). Inverse modeling in HeFTy is based on an iterative Monte Carlo approach which tests an assigned number of t-T paths to assess the goodness-of-fit (GOF) between the input data and the predicted date and track length distributions. This inverse thermal history modeling generates "acceptable" and "good" t-T paths. An "acceptable" path indicates that the modeled thermal history cannot be excluded by the measured data and corresponds to a GOF value of 0.05 or higher. A "good" path is supported by the measured data and corresponds to a

10.1029/2020TC006416

Table 3
Summary of AHe Results With Individual Grain Dates and Mean AHe Dates, Where Applicable

Sample name	Traverse	Elevation (m)	Latitude	Longitude	Rs (um)	Corrected date (Ma)	± 1σ	eU (ppm)	Arithmetic mean (Ma)	± 1 SD	1σ SSD (%)	# GE
HS-1-390_Ap1	HS-1	390	34.5189	109.9585	46.45	5.33	0.62	2.53				
HS-1-390_Ap2	HS-1	390	34.5189	109.9585	42.13	5.23	0.46	2.72				
HS-1-390_Ap3	HS-1	390	34.5189	109.9585	42.47	9.26	0.27	11.18				
HS-1-390_Ap4	HS-1	390	34.5189	109.9585	55.57	23.35	0.41	13.36				
Mean Date									-	-	-	-
HS-1-1840_Ap2	HS-1	1840	34.4418	109.9716	61.12	45.46	0.49	8.50				
HS-1-1840_Ap3	HS-1	1840	34.4418	109.9716	85.38	44.73	0.44	11.09				
HS-1-1840_Ap4	HS-1	1840	34.4418	109.9716	80.15	54.12	0.58	21.37				
Mean Date									**48**	**5**	11	0
HS-2-590_Ap1	HS-2	590	34.4993	110.5506	49.83	39.65	0.78	82.53				
HS-2-590_Ap2	HS-2	590	34.4993	110.5506	53.08	36.62	0.72	69.07				
HS-2-590_Ap3	HS-2	590	34.4993	110.5506	44.79	35.84	0.71	72.01				
HS-2-590_Ap4	HS-2	590	34.4993	110.5506	51.50	23.53	0.49	64.61				
Mean Date									**34**	**7**	21	0
HS-2-800_Ap1	HS-2	800	34.4707	110.5360	56.62	58.78	0.89	9.32				
HS-2-800_Ap2	HS-2	800	34.4707	110.5360	52.85	112.25	1.61	24.14				
HS-2-800_Ap4	HS-2	800	34.4707	110.5360	52.40	219.61	3.23	11.56				
HS-2-800_Ap5	HS-2	800	34.4707	110.5360	52.10	205.00	3.12	19.54				
Mean Date									-	-	-	-
HS-2-964_Ap1	HS-2	964	34.4586	110.5371	52.41	29.23	0.51	12.40				
HS-2-964_Ap2	HS-2	964	34.4586	110.5371	45.55	26.02	0.57	14.32				
HS-2-964_Ap3	HS-2	964	34.4586	110.5371	47.48	119.06	2.05	8.35				
HS-2-964_Ap4	HS-2	964	34.4586	110.5371	61.16	36.75	0.67	11.81				
Mean Date									**31**	**6**	18	1
HS-2-1150_Ap1	HS-2	1150	34.4624	110.5150	54.12	128.78	1.38	11.88				
HS-2-1150_Ap3	HS-2	1150	34.4624	110.5150	66.15	50.66	0.56	9.13				
HS-2-1150_Ap4	HS-2	1150	34.4624	110.5150	47.31	41.61	0.48	11.12				
~~*Mean Date*~~									-	-	-	-
HS-2-1592_Ap1	HS-2	1592	34.4584	110.5079	75.99	102.23	1.04	14.22				
HS-2-1592_Ap2	HS-2	1592	34.4584	110.5079	56.45	64.59	0.68	13.42				
HS-2-1592_Ap3	HS-2	1592	34.4584	110.5079	71.70	40.75	0.44	11.72				
HS-2-1592_Ap4	HS-2	1592	34.4584	110.5079	85.20	52.91	0.55	14.03				
~~*Mean Date*~~									-	-	-	-
HS-2-1810_Ap1	HS-2	1810	34.4553	110.5052	57.60	88.13	0.91	13.09				
HS-2-1810_Ap2	HS-2	1810	34.4553	110.5052	55.64	1049.98	12.09	12.43				
HS-2-1810_Ap3	HS-2	1810	34.4553	110.5052	46.48	224.60	2.40	15.95				
HS-2-1810_Ap4	HS-2	1810	34.4553	110.5052	64.65	62.67	0.66	12.99				
~~*Mean Date*~~									-	-	-	-
HS-2-2100_Ap2	HS-2	2100	34.4500	110.5085	86.32	55.51	0.59	11.36				
HS-2-2100_Ap3	HS-2	2100	34.4500	110.5085	48.26	62.18	0.73	7.88				
HS-2-2100_Ap4	HS-2	2100	34.4500	110.5085	53.03	62.50	0.69	12.55				
HS_2_2100_Ap5	HS-2	2100	34.4500	110.5085	48.85	72.68	0.99	11.92				

Table 3
Continued

Sample name	Traverse	Elevation (m)	Latitude	Longitude	Rs (um)	Corrected date (Ma)	± 1σ	eU (ppm)	Arithmetic mean (Ma)	± 1 SD	1σ SSD (%)	# GE
Mean Date									**63**	**7**	11	0
ZT-1-476_Ap1	ZT-1	476	34.8532	110.5066	70.35	23.49	0.34	40.26				
ZT-1-476_Ap2	ZT-1	476	34.8532	110.5066	57.94	50.36	0.73	37.33				
ZT-1-476_Ap3	ZT-1	476	34.8532	110.5066	133.02	43.44	0.47	38.18				
ZT-1-476_Ap4	ZT-1	476	34.8532	110.5066	100.12	39.90	0.44	26.70				
Mean Date									**45**	*5*	12	1
ZT-1-750_Ap1	ZT-1	750	34.8424	110.5037	44.17	33.49	0.43	27.56				
ZT-1-750_Ap2	ZT-1	750	34.8424	110.5037	39.56	255.54	2.83	49.36				
ZT-1-750_Ap3	ZT-1	750	34.8424	110.5037	61.76	43.05	0.52	18.78				
ZT-1-750_Ap4	ZT-1	750	34.8424	110.5037	49.26	36.78	0.44	25.91				
Mean Date									**38**	**5**	13	1
ZT-1-1022_Ap1	ZT-1	1022	34.8321	110.5040	68.53	58.89	0.91	31.50				
ZT-1-1022_Ap2	ZT-1	1022	34.8321	110.5040	66.51	51.78	0.80	37.05				
ZT-1-1022_Ap3	ZT-1	1022	34.8321	110.5040	54.20	47.72	0.76	37.17				
ZT-1-1022_Ap4	ZT-1	1022	34.8321	110.5040	50.71	49.88	0.78	33.88				
Mean Date									**52**	**5**	9	0
ZT-1-1240_Ap1	ZT-1	1240	34.8299	110.5037	73.90	87.38	1.43	27.39				
ZT-1-1240_Ap2	ZT-1	1240	34.8299	110.5037	65.83	60.25	0.99	35.67				
ZT-1-1240_Ap3	ZT-1	1240	34.8299	110.5037	49.81	85.84	1.43	23.09				
ZT-1-1240_Ap4	ZT-1	1240	34.8299	110.5037	98.47	104.60	1.75	32.47				
Mean Date									**78**	**15**	20	1
ZT-1-1560_Ap1	ZT-1	1560	34.8160	110.5097	70.40	112.60	2.79	29.26				
ZT-1-1560_Ap2	ZT-1	1560	34.8160	110.5097	100.35	101.83	2.52	31.82				
ZT-1-1560_Ap3	ZT-1	1560	34.8160	110.5097	68.50	123.86	3.05	34.18				
ZT-1-1560_Ap4	ZT-1	1560	34.8160	110.5097	107.14	106.78	1.18	35.39				
Mean Date									**111**	**10**	9	0
ZT-2-448_Ap1	ZT-2	448	34.9618	111.0359	61.29	35.62	0.49	98.80				
ZT-2-448_Ap2	ZT-2	448	34.9618	111.0359	77.17	39.76	0.55	123.72				
ZT-2-448_Ap3	ZT-2	448	34.9618	111.0359	76.61	24.76	0.35	99.35				
ZT-2-448_Ap4	ZT-2	448	34.9618	111.0359	73.05	40.17	0.56	78.73				
Mean Date									**35**	**7**	21	0
ZT-2-674_Ap1	ZT-2	674	34.9499	111.0517	99.13	29.16	0.39	34.60				
ZT-2-674_Ap2	ZT-2	674	34.9499	111.0517	75.84	25.60	0.44	24.82				
ZT-2-674_Ap3	ZT-2	674	34.9499	111.0517	76.14	37.57	0.63	67.51				
ZT-2-674_Ap4	ZT-2	674	34.9499	111.0517	75.79	23.04	0.44	7.41				
Mean Date									**26**	**3**	12	1
ZT-2-930_Ap1	ZT-2	930	34.9444	111.0675	68.61	45.63	0.76	62.61				
ZT-2-930_Ap2	ZT-2	930	34.9444	111.0675	64.10	50.86	0.87	43.77				
ZT-2-930_Ap3	ZT-2	930	34.9444	111.0675	52.56	45.66	0.77	54.41				
ZT-2-930_Ap4	ZT-2	930	34.9444	111.0675	86.47	46.38	0.77	45.88				
Mean Date									**47**	**3**	5	0
ZT-3-528_Ap1	ZT-3	528	35.2152	111.3155	60.27	131.73	2.46	121.10				

Table 3
Continued

Sample name	Traverse	Elevation (m)	Latitude	Longitude	Rs (um)	Corrected date (Ma)	± 1σ	eU (ppm)	Arithmetic mean (Ma)	± 1 SD	1σ SSD (%)	# GE
ZT-3-528_Ap2	ZT-3	528	35.2152	111.3155	60.83	96.48	1.82	50.69				
ZT-3-528_Ap3	ZT-3	528	35.2152	111.3155	49.75	45.27	0.93	16.99				
ZT-3-528_Ap4	ZT-3	528	35.2152	111.3155	64.05	15.37	0.44	6.35				
Mean Date									-	-	-	-
ZT-3-806_Ap1	ZT-3	806	35.1944	111.3566	140.49	25.58	0.42	10.37				
ZT-3-806_Ap2	ZT-3	806	35.1944	111.3566	106.93	36.45	0.59	9.27				
ZT-3-806_Ap3	ZT-3	806	35.1944	111.3566	100.21	46.67	0.75	11.02				
ZT-3-806_Ap4	ZT-3	806	35.1944	111.3566	113.23	43.85	0.72	6.73				
Mean Date									**42**	*5*	12	1
ZT-3-1090_Ap1	ZT-3	1090	35.1925	111.3820	90.27	77.80	1.19	16.32				
ZT-3-1090_Ap2	ZT-3	1090	35.1925	111.3820	93.60	55.34	0.97	5.09				
ZT-3-1090_Ap3	ZT-3	1090	35.1925	111.3820	98.25	90.51	1.41	12.28				
ZT-3-1090_Ap4	ZT-3	1090	35.1925	111.3820	110.46	101.06	2.47	19.64				
~~*Mean Date*~~									-	-	-	-
ZT-3-1346_Ap1	ZT-3	1346	35.1917	111.3915	60.62	78.80	1.60	7.67				
ZT-3-1346_Ap2	ZT-3	1346	35.1917	111.3915	45.35	50.85	1.08	9.56				
ZT-3-1346_Ap3	ZT-3	1346	35.1917	111.3915	41.76	58.02	1.49	9.85				
ZT-3-1346_Ap4	ZT-3	1346	35.1917	111.3915	49.05	288.52	5.89	9.89				
~~*Mean Date*~~									-	-	-	-
TS-1-1241_Ap1	TS-1	1241	36.6742	111.9134	64.28	27.66	0.32	17.45				
TS-1-1241_Ap2	TS-1	1241	36.6742	111.9134	64.36	28.01	0.33	16.57				
TS-1-1241_Ap3	TS-1	1241	36.6742	111.9134	61.37	22.46	0.27	26.37				
TS-1-1241_Ap4	TS-1	1241	36.6742	111.9134	90.20	22.38	0.27	13.72				
Mean Date									**25**	**3**	12	0
TS-1-1584_Ap1	TS-1	1584	36.6553	111.9440	49.80	38.88	0.49	222.02				
TS-1-1584_Ap2	TS-1	1584	36.6553	111.9440	53.41	43.95	0.57	149.98				
TS-1-1584_Ap3	TS-1	1584	36.6553	111.9440	59.00	39.69	0.52	151.30				
TS-1-1584_Ap4	TS-1	1584	36.6553	111.9440	44.90	33.55	0.46	78.42				
Mean Date									**39**	**4**	11	0
TS-1-2034_Ap1	TS-1	2034	36.6515	111.9697	81.45	37.85	0.47	36.71				
TS-1-2034_Ap2	TS-1	2034	36.6515	111.9697	102.32	30.83	0.42	34.39				
TS-1-2034_Ap3	TS-1	2034	36.6515	111.9697	83.09	33.61	0.46	46.77				
TS-1-2034_Ap4	TS-1	2034	36.6515	111.9697	81.12	42.84	0.59	58.10				
Mean Date									**36**	**5**	14	0
TS-2-847_Ap1	TS-2	847	36.6052	111.8741	78.17	84.93	2.14	10.44				
TS-2-847_Ap2	TS-2	847	36.6052	111.8741	58.29	57.50	1.45	22.11				
TS-2-847_Ap3	TS-2	847	36.6052	111.8741	63.15	65.19	1.68	9.82				
TS-2-847_Ap4	TS-2	847	36.6052	111.8741	54.39	70.94	1.82	37.58				
Mean Date									**70**	**12**	17	0
TS-2-1245_Ap1	TS-2	1245	36.6050	111.9516	105.98	31.15	0.39	11.07				
TS-2-1245_Ap2	TS-2	1245	36.6050	111.9516	89.38	51.08	0.57	18.55				
TS-2-1245_Ap3	TS-2	1245	36.6050	111.9516	78.06	38.25	0.50	20.43				

Table 3
Continued

Sample name	Traverse	Elevation (m)	Latitude	Longitude	Rs (um)	Corrected date (Ma)	± 1σ	eU (ppm)	Arithmetic mean (Ma)	± 1 SD	1σ SSD (%)	# GE
TS-2-1245_Ap4	TS-2	1245	36.6050	111.9516	96.95	38.12	0.50	16.90				
Mean Date									**36**	**4**	11	1
TS-2-1456_Ap1	TS-2	1456	36.6132	111.9857	71.80	22.21	0.43	43.97				
TS-2-1456_Ap2	TS-2	1456	36.6132	111.9857	63.81	30.44	0.55	29.42				
TS-2-1456_Ap3	TS-2	1456	36.6132	111.9857	56.34	24.06	0.56	11.83				
TS-2-1456_Ap4	TS-2	1456	36.6132	111.9857	57.39	17.80	0.40	12.74				
Mean Date									**21**	**3**	15	1
CLS-Sst-1311_Ap1	CLS	1311	37.8770	112.3921	43.50	24.61	1.56	11.32				
CLS-Sst-1311_Ap2	CLS	1311	37.8770	112.3921	36.84	33.80	0.83	28.48				
CLS-Sst-1311_Ap3	CLS	1311	37.8770	112.3921	76.50	31.15	0.58	19.35				
Mean Date									**30**	**5**	16	0
CLS-Sst-1612_Ap1	CLS	1612	37.8334	112.3072	92.12	27.86	0.54	38.59				
CLS-Sst-1612_Ap2	CLS	1612	37.8334	112.3072	102.96	26.57	0.50	11.80				
CLS-Sst-1612_Ap3	CLS	1612	37.8334	112.3072	64.43	31.63	0.65	18.79				
CLS-Sst-1612_Ap4	CLS	1612	37.8334	112.3072	62.28	29.89	0.61	21.58				
Mean Date									**29**	**2**	8	0
CLS-Sst-1376_Ap1	CLS	1376	37.7100	112.2172	69.75	36.23	0.71	11.27				
CLS-Sst-1376_Ap2	CLS	1376	37.7100	112.2172	59.34	25.16	0.48	33.34				
CLS-Sst-1376_Ap3	CLS	1376	37.7100	112.2172	61.69	13.28	1.16	4.57				
CLS-Sst-1376_Ap4	CLS	1376	37.7100	112.2172	57.01	37.71	0.89	9.03				
Mean Date									**33**	**7**	21	1
CLS-BSMT-1062_Ap1	CLS	1062	38.0322	111.9538	45.26	84.00	1.67	54.70				
CLS-BSMT-1062_Ap2	CLS	1062	38.0322	111.9538	45.34	113.86	2.22	50.92				
CLS-BSMT-1062_Ap3	CLS	1062	38.0322	111.9538	61.02	108.05	2.10	67.63				
CLS-BSMT-1062_Ap4	CLS	1062	38.0322	111.9538	39.36	86.88	1.68	114.67				
Mean Date									**98**	**15**	15	0
CLS-BSMT-1720_Ap1	CLS	1720	38.0073	111.5055	44.20	100.34	4.03	7.18				
CLS-BSMT-1720_Ap2	CLS	1720	38.0073	111.5055	46.68	966.04	18.97	9.97				
CLS-BSMT-1720_Ap3	CLS	1720	38.0073	111.5055	41.10	114.22	2.60	12.74				
CLS-BSMT-1720_Ap4	CLS	1720	38.0073	111.5055	43.99	561.30	12.14	10.85				
Mean Date									-	-	-	-
NLS-BSMT-1270_Ap1	NLS	1270	38.6259	112.4861	84.04	607.89	11.87	7.39				
NLS-BSMT-1270_Ap2	NLS	1270	38.6259	112.4861	54.62	376.90	7.99	8.24				
NLS-BSMT-1270_Ap3	NLS	1270	38.6259	112.4861	76.64	197.98	3.81	18.61				
NLS-BSMT-1270_Ap4	NLS	1270	38.6259	112.4861	56.16	162.83	3.24	22.43				
~~*Mean Date*~~									-	-	-	-
NLS-BSMT-1630_Ap1	NLS	1630	38.6422	112.4307	76.07	145.43	3.13	9.72				
NLS-BSMT-1630_Ap2	NLS	1630	38.6422	112.4307	80.19	101.43	2.10	13.78				
~~*Mean Date*~~									-	-	-	-
XZ-BSMT-589_Ap1	XZ	589	38.4126	113.3527	93.42	28.30	0.54	10.80				
XZ-BSMT-589_Ap2	XZ	589	38.4126	113.3527	107.59	34.77	0.65	9.77				
XZ-BSMT-589_Ap3	XZ	589	38.4126	113.3527	93.24	37.09	0.70	9.82				

Table 3
Continued

Sample name	Traverse	Elevation (m)	Latitude	Longitude	Rs (um)	Corrected date (Ma)	± 1σ	eU (ppm)	Arithmetic mean (Ma)	± 1 SD	1σ SSD (%)	# GE
XZ-BSMT-589_Ap4	XZ	589	38.4126	113.3527	103.13	40.08	0.74	13.23				
Mean Date									**35**	**5**	14	0
XZ-BSMT-692_Ap1	XZ	692	38.3333	113.3467	49.57	41.61	1.04	8.09				
XZ-BSMT-692_Ap2	XZ	692	38.3333	113.3467	46.57	83.10	1.64	12.77				
XZ-BSMT-692_Ap3	XZ	692	38.3333	113.3467	61.10	89.11	1.97	5.54				
~~*Mean Date*~~									-	-	-	-
XZ-SSt-843_Ap1	XZ	843	38.2487	113.3089	75.01	23.11	0.42	352.16				
XZ-SSt-843_Ap2	XZ	843	38.2487	113.3089	72.85	50.18	0.99	14.15				
XZ-SSt-843_Ap3	XZ	843	38.2487	113.3089	74.11	111.51	1.97	15.05				
XZ-SSt-843_Ap4	XZ	843	38.2487	113.3089	82.13	44.52	0.81	98.36				
~~*Mean Date*~~									-	-	-	-

Note. Single grains excluded from mean date calculation shown by a strike-through line under the "sample name" column. Mean dates are reported if 3 or more grains were used to calculate the mean and if the 1σ SSD (%) <~20%. If a mean date is not recorded, the "mean date" is shown with a strike-through line, under the "sample name" column. eU (ppm): includes U, Th, and Sm. #GE: number of grains excluded for mean date.
Abbreviations: AHe, apatite (U-Th-Sm)/He; SD, standard deviation; SSD, sample standard deviation.

mean GOF value of ≥0.50. Inverse models in HeFTy were built for individual AFT samples, including ~20 crystal dates, ≥30 horizontal confined track length (HCTLs) measurements, and track etch pit diameters (D_{par}). We also tested inverse models in HeFTy that combined the AFT and single apatite grain AHe data, but the models generally produced no "acceptable" paths and are not discussed further. Simulations were initially run for 25,000 paths to test for ≥100 good paths. If < 100 good paths were found, models were rerun to test 50,000 paths. See supplementary information for additional details on modeling constraints.

We also undertook inverse modeling using QTQt software (version 5.7.0; Gallagher, 2012) to produce likely t-T histories for two elevation transects in the Huashan and Zhongtiaoshan. Inverse modeling in QTQt uses a Bayesian Markov Chain Monte Carlo approach where a user can input the thermochronometric data and define t-T constraints. The model outputs are a population of acceptable thermal histories based on a posterior probability (Gallagher, 2012). "Expected" paths, as shown here, represent the weighted mean thermal history from the posterior distribution. QTQt is particularly useful for modeling multiple samples as part of an elevation transect. This approach, however, assumes that all samples experienced the same thermal history and that the relative structural relationship between samples remained unchanged since the initiation of the modeled thermal history (i.e., samples occupy the same fault block). For simplicity, we only constructed these models for multi-sample transects characterized by positive date-elevation correlations. Inverse models include the single grain AFT dates, track length distributions, and D_{par} measurements for all samples within the elevation transect, and assume a geothermal gradient of 25 ± 10 °C/km. All AFT samples within the transects were included in the model regardless of the number of measured HCTLs, although most of the samples are characterized by > 20 HCTLs. The most likely t-T reconstructions are plotted alongside the predicted AFT dates and modeled track length distributions. See supplementary information for elaboration on modeling constraints.

4. Results

New AFT and AHe data results are subdivided based on the sampled range and elevation transect. These ranges are, from south to north, the Huashan, Zhongtiaoshan, Huoshan, Taihangshan, and Lüliangshan. All AFT samples pass the chi-square test, suggesting a single population of grains (Table 2; Galbraith, 2005). Single grain AHe dates, mean AHe dates, and single-grain analyses omitted from mean date calculations are shown in Table 3.

4.1. Huashan

Nine AFT samples from two elevation transects were collected in the Huashan. The western elevation transect (HS-1) consists of only two samples, including a low elevation sample at ~390 m near the Huashan fault (HS-1-390) and an upper elevation sample (HS-1-1840) at ~1,840 m. We analyzed two samples from this transect to compare the results to a nearby published data set (Figures 3 and 5a; J. Liu et al., 2013). HS-1-390 and HS-1-1840 exhibit overlapping AFT dates of, respectively, 41 ± 7 Ma and 46 ± 5 Ma. Both samples yielded a statistically insignificant number of HCTLs (≤5), but the mean measured lengths are ~14.3–14.4 μm. Four single grain AHe dates for HS-1-390 range from ca. 23–5 Ma with a positive date-eU correlation and a mean AHe date of 10.8 ± 8.6 Ma, but the mean date is disregarded because of significant intrasample AHe date dispersion and a 1σ sample standard deviation > 20% (e.g., Flowers & Kelley, 2011). The two youngest AHe dates of ca. 5 Ma are characterized by eU values of <3 ppm and a relative uncertainty of >8% (1σ/date), higher compared to other the other AHe dates presented with an average uncertainty of <~2.5% (supplementary AHe data table). Three single grain AHe dates for HS-1-1840 range from ca. 54 to 45 Ma with a mean date of 48 ± 5 Ma, a 1σ sample standard deviation of 11%, and a weak positive date-eU correlation (Figure 5a).

The eastern elevation transect (HS-2) includes seven samples collected at elevations ranging from ~590 m to ~2,100 m. AFT dates range from ca. 47–33 Ma and exhibit an overall positive date-elevation correlation (Figure 5b). Six of the seven samples yielded ≥14 HCTLs, characterized by mean track lengths of ~13.1–14.6 μm, track length standard deviations of 0.7–1.12 μm, and a mixed to unimodal track length distribution (e.g., Gleadow, Duddy, Green, & Hegarty, 1986). The HS-2 transect includes three to four AHe grain dates per sample for a total of 27 analyses, however, only three of the seven samples met the criteria to calculate a mean AHe date. Single grain AHe dates <200 Ma range from ca. 129 to 24 Ma and mean AHe dates range from ca. 63 to 34 Ma (Table 3). Sample HS-2-590 shows a positive date-eU correlation with eU values ranging from ~65–83 ppm. In comparison, intrasample date dispersion for samples of this transect are not correlated with eU and eU values are within a narrow range at values of <25 ppm (Figure 5b).

4.2. Zhongtiaoshan

Twelve samples were collected from three elevation transects in the Zhongtiaoshan. The western transect (ZT-1; Figure 3) consists of five samples with AFT dates that range from ca. 95 to 45 Ma and exhibit a positive date-elevation correlation (Figure 5c). Mean track lengths range from ~12.7 to 13.6 μm and mean lengths tend to decrease with elevation, except for the uppermost elevation sample (ZT-1-1560). The lowest elevation sample (ZT-1-476) is associated with the longest mean track length. Track length standard deviations range from 1.1 to 1.7 μm and are associated with mixed and unimodal length distributions. The ZT-1 transect includes four AHe single grain dates per sample for a total of 20 analyses. AHe dates from ZT-1 generally increase with elevation and range from ca. 124 to 23 Ma (Figure 5c), and the mean AHe dates from the two lowest elevation samples (ZT-1-476 and ZT-1-750) are, respectively, ca. 45 and 38 Ma, versus the upper elevation sample (ZT-1-1560) with a mean date of ca. 111 Ma.

An increase in date with elevation is also observed with the youngest single grain dates across the transect.

The central elevation transect (ZT-2; Figure 3) consists of three samples from elevations between ~448 m and ~930 m. No AFT data were collected for this transect. The ZT-2 transect includes four AHe single grain dates per sample for a total of 12 analyses. Single grain dates range from ca. 23 to 51 Ma with mean AHe dates of ca. 47–26 Ma (Figure 5d). The lowest and medial elevation samples (ZT-2-448 and ZT-2-674) yielded mean AHe dates of, respectively, 35 ± 7 Ma and 26 ± 3 Ma and overlap at a 1σ standard deviation. The oldest mean AHe date of ca. 47 ± 3 Ma is associated with the highest elevation sample (ZT-2-930).

The eastern transect (ZT-3; Figure 2) consists of four samples from elevations between ~528 m and ~1,346 m. The four AFT dates range from ca. 96 to 72 Ma and exhibit a positive date-elevation correlation (Figure 5e), and mean track lengths range from ~12.8 to 13.4 μm with track length standard deviations of ~1.1–1.98 μm. No systematic increase in mean track length is observed with elevation and track lengths tend to exhibit a mixed to bimodal distribution. The ZT-3 transect includes four single grain dates per sample. The lowest elevation sample (ZT-3-528) is characterized by single grain AHe dates ranging from ca. 132–15 Ma and a positive date-eU correlation. The upper three elevation samples (ZT-3-806, -1090, -1346) yielded single grain

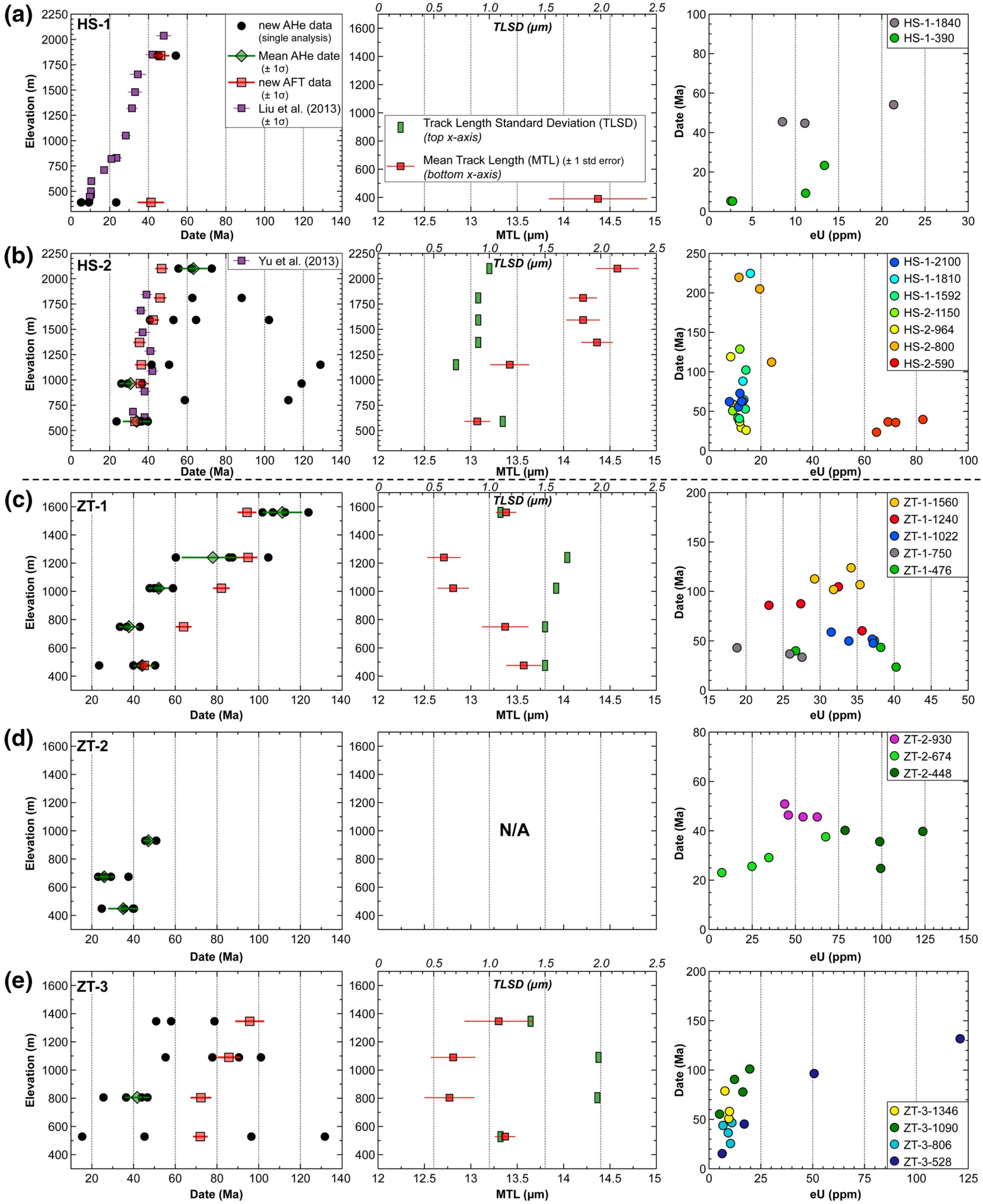

Figure 5. New AHe and AFT data for the Huashan and Zhongtiaoshan transects: (a) HS-1, (b) HS-2, (c) ZT-1, (d) ZT-2, and (e) ZT-3. Date versus elevation (left column); mean track length (MTL) and track length standard deviation (TLSD) versus elevation (center column); and eU versus date (right column). Note the different x-axis scales associated with eU values. AFT, apatite fission track; AHe, apatite U-Th-Sm/He.

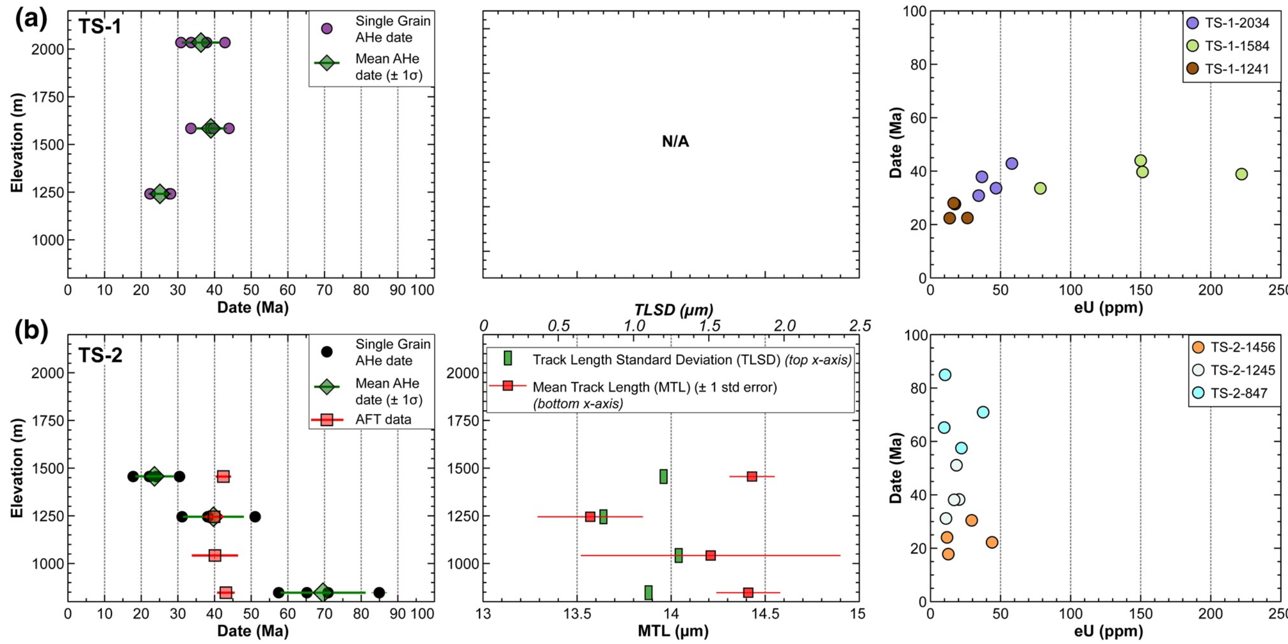

Figure 6. New AHe and AFT data for transects (a) TS-1 and (b) TS-2 in the Huoshan. Date versus elevation (left column); mean track length (MTL) and track length standard deviation (TLSD) versus elevation (center column); and eU versus date (right column).

AHe dates ranging from ca. 101 to 26 Ma (after omitting an anomalously old date; Table 3) and ZT-3-806 satisfied the criteria to report a mean AHe date of 42 ± 5 Ma. ZT-3-528 and ZT-3-1090 are characterized by positive date-eU correlations with eU values ranging from, respectively, ∼6–121 ppm and ∼5–20 ppm.

4.3. Huoshan

Samples from the Huoshan are from two transects (TS-1 and TS-2). TS-1 includes three samples and 12 single grain AHe dates which range from ca. 44–22 Ma (Figure 6a). Samples from elevations of 1,241, 1,584, and 2,034 m yielded mean AHe dates of, respectively, ca. 25, 39, and 36 Ma with the youngest AHe mean date associated with the lowest elevation sample (TS-1-1241).

TS-2 includes four AFT dates and three samples with four single grain AHe dates (Figure 6b). AFT dates range from ca. 43 to 40 Ma with no systematic correlation with elevation. Single grain AHe dates range from ca. 85 to 18 Ma. Samples from elevations of 847, 1,245, and 1,456 m yielded mean AHe dates of, respectively, ca. 70, 36, and 21 Ma. These mean AHe dates show a negative date-elevation correlation and the mean AHe date for TS-2-847 is older, or inverted, relative to its AFT date.

4.4. Lüliangshan

Three upper Paleozoic-Triassic sandstone and four basement samples were collected from the Lüliangshan. No AFT data were collected for these samples (Table 1). The three sandstone samples (CLS-SSt-1311, -1376, -1612) include three to four analyzed grains per sample for a total of 11 AHe dates, and mean AHe dates of ca. 33–29 Ma (Table 2; Figure 7a). The four basement samples include two samples from the central Lüliangshan (CLS-BSMT-1062, -1720) and two from the northern Lüliangshan (NLS-BSMT-1270, -1630). Single grain AHe dates exhibit significant intra-sample variability, but weak to no date-eU correlations (Figure 7a). The single grain AHe dates range from 163 to 84 Ma after omitting anomalously old dates of >180 Ma ($n_{omitted} = 5$). Sample CLS-BSMT-1062 is the only basement sample with ≥3 grains and a 1σ sample standard deviation of <20% used to calculate a mean AHe date of 98 ± 15 Ma. These AHe data show no clear correlation between date and elevation.

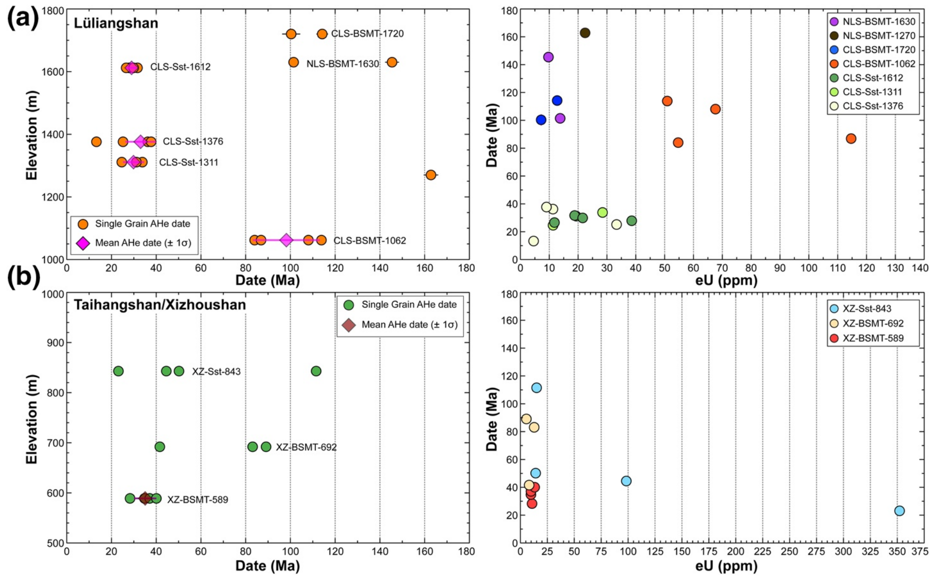

Figure 7. New AHe data for the (a) Lüliangshan and (b) Taihangshan. Date versus elevation (left column) and eU versus date (right column). AFT, apatite fission track; AHe, apatite U-Th-Sm/He.

4.5. Taihangshan

Three samples, including two basement and one lower Paleozoic sandstone, were collected from the Taihangshan along a tributary to the Hutuo River (Figure 4). The two basement samples are, XZ-BSMT-589, which consists of four single grain AHe dates ranging from ca. 40 to 28 Ma and a mean AHe date of ca. 35 ± 5 Ma, and XZ-BSMT-692, which includes three dispersed single grain dates of ca. 42, 83, and 89 Ma (Figure 7b). The lower Paleozoic sandstone sample (XZ-SSt-843) yielded four single grain AHe dates ranging from ca. 112 to 23 Ma and exhibits a negative date-eU correlation, possibly due to excess He in the younger grains by He implantation (e.g., Murray et al., 2014).

5. Summary of Data Compilation Results (New and Published)

New and published low-temperature thermochronologic data are summarized for four regional transects (Figures 3 and 4). These transects include, from south to north: (1) transect 1 across the Huashan, Zhongtiaoshan, southeast Ordos Block, and the Huoshan (Figure 8a); (2) transect 2 across the central Lüliangshan and Taihangshan (Figure 8b); (3) transect 3 across the northern Lüliangshan and Xizhoushan (Figure 8c); and (4) transect 4 across the Hengshan, Wutaishan, and northern Taihangshan (Figure 8d). Data in this compilation include AHe, AFT, zircon U-Th/He (ZHe), and zircon fission track (ZFT) data. Assuming a 10°C/Myr cooling rate, the ZHe and ZFT thermochronometers have effective closure temperatures of, respectively, ∼180°C and >∼230°C, although variations in closure temperature may exist because of differences in crystal size, magnitude of radiation damage, and cooling rates (e.g., Reiners & Brandon, 2006). Published AFT and ZFT data are presented only for samples with chi-square values of ≥5%. Refer to the supporting information for additional details, including sources, for the compiled data.

In transect 1 of the southern rift, published AFT dates range from ca. 65 to 10 Ma and new AFT dates (including those from Clinkscales et al., 2020) range from ca. 96 to 33 Ma with a population cluster at ca. 50–30 Ma. In comparison, mean AHe dates range from 111 to 25 Ma with the greatest number of samples between ca. 50 and 30 Ma (Figure 9a). In the southwestern Huashan, by the Luonan fault (Figure 3), AFT dates range from ca. 57 to 20 Ma (e.g., Enkelmann et al., 2006; H. Chen et al., 2015). These closely overlap with published AFT and ZFT dates from the eastern Huashan (Figure 3), which range, respectively, from ca. 42–36 Ma and ca. 50–40 Ma (X. Yu, Liu, Zhang, et al., 2013; Y.-T. Wang et al., 2019), and also with new AFT dates of ca. 47–33 Ma (Figures 5b and 8a). AFT dates of ca. 10 Ma are known from the northwestern Huashan (J. Liu et al., 2013). To test if the Miocene AFT dates in the northwestern Huashan were consistent

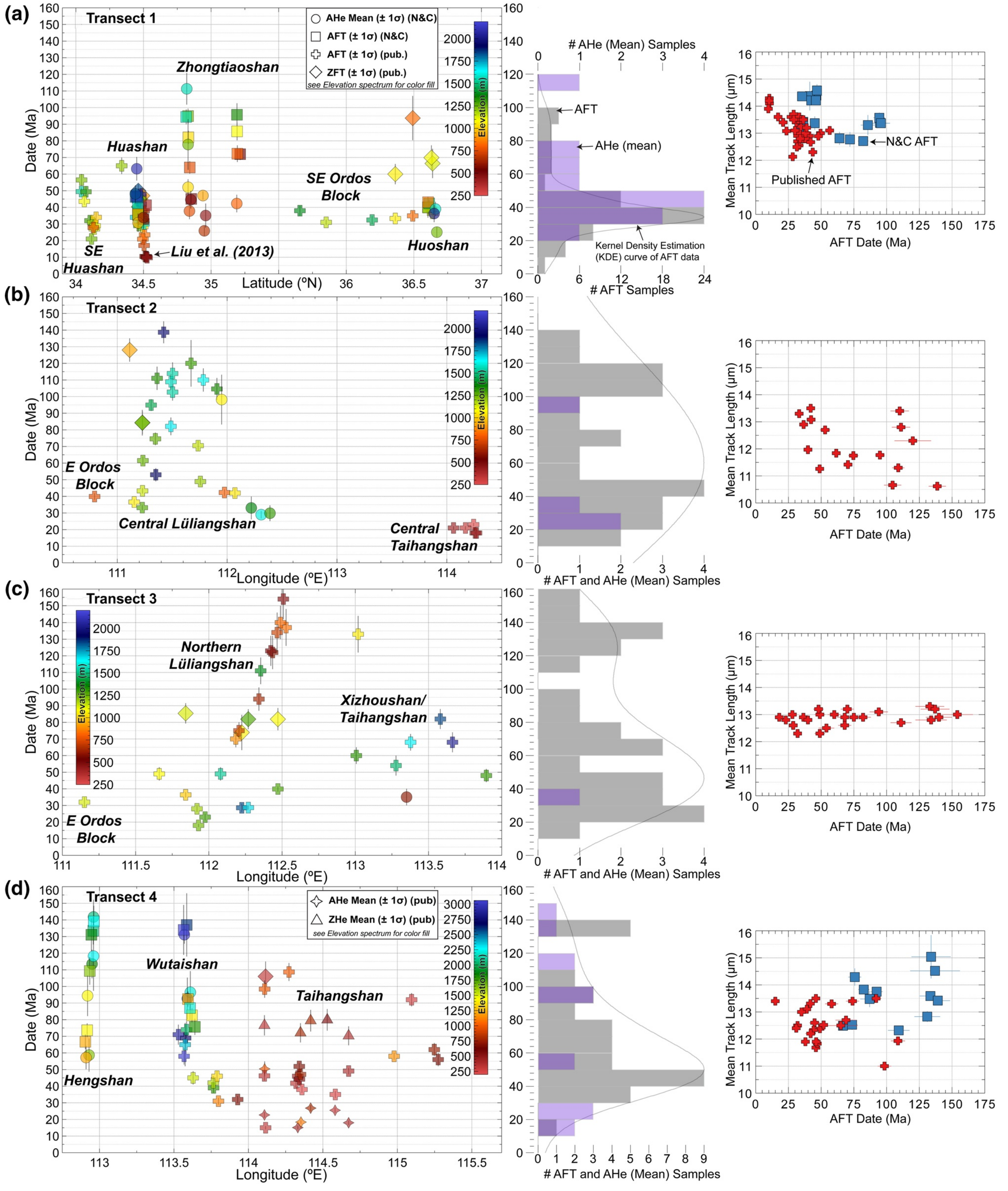

Figure 8. Four data transects across the Shanxi Rift, including new and previously published thermochronologic data. (a) Transect A includes the south and south-central rift zone. Refer to Figure 3 for sample locations in transect 1. (b–d) Transects 2–4 are outlined in Figure 4. Sample locations (latitude for a; longitude for b–d) versus date shown in the left column; histograms of AFT and mean AHe dates for each transect and a kernel density estimation (KDE) curve to outline the distribution of AFT data in the center column; and AFT date versus mean track length measurements for each transect in the right column. N&C includes new data from this study and published data from Clinkscales et al. (2020). References and additional information for published thermochronologic data are provided in the supporting information. AFT, apatite fission track; AHe, apatite U-Th-Sm/He.

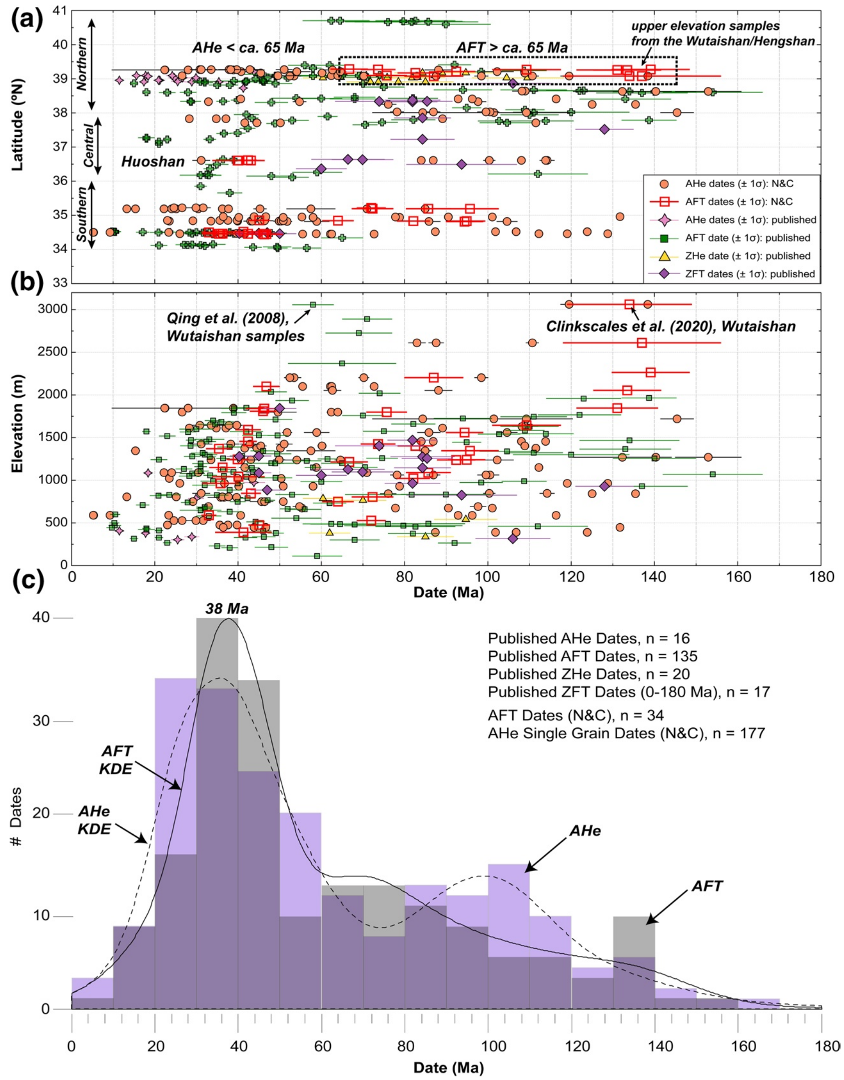

Figure 9. Compilation of low-temperature thermochronologic dates versus (a) latitude and (b) elevation. (c) Histogram and kernel density estimation (KDE) plot of published and new AFT and AHe data. N&C includes new data from this study and published data from Clinkscales et al. (2020). AFT, apatite fission track; AHe, apatite U-Th-Sm/He.

along strike, we collected new AFT and AHe data for a sample at a low elevation and similar structural position as reported by J. Liu et al. (2013). The new data, in comparison, yielded an AFT date of ca. 40 Ma and AHe dates of ca. 23–5 Ma (Figure 5a).

Transect 1 also includes the region north of the Weihe Graben in the southeastern Ordos block, where samples from Paleozoic–Triassic strata yielded AFT dates of ca. 40–30 Ma and ZFT dates of ca. 94–64 Ma (X. Li & Song, 2010). In comparison AFT dates from the Huoshan, at a similar latitude to the Ordos samples, range from 43–40 Ma (Figure 8a).

In the central Lüliangshan of transect 2, published AFT dates range from ca. 139 to 33 Ma and new AHe mean dates cluster at ca. 30 Ma (Figure 8b). Three ZFT dates in the central Lüliangshan include two dates at ca. 84 Ma (X. Li & Song, 2010) and a single date at ca. 128 Ma (J. Zhao et al., 2016). AFT dates near the Eastern Taihangshan fault, in the easternmost central Taihangshan (Figure 2), range from 23 to 18 Ma (Figure 8b).

In the northern Lüliangshan of transect 3, published AFT dates range from ca. 154 to 18 Ma with a population of AFT dates of ca. 155–120 Ma, notably located in the core of a basement-involved anticline (Cao et al., 2015, Figures 4 and 8c). In contrast, AFT dates of ca. 75–70 Ma are from detrital apatite grains in Triassic–Jurassic strata (J. Zhao et al., 2016) in the core of a syncline to the northwest of the basement-involved anticline (Figure 3). There does not appear to be a clear structural explanation for the occurrence of AFT dates <50 Ma in the northern Lüliangshan; however, an AFT date of ca. 32 Ma (S. B. Li et al., 2015) is observed in upper Paleozoic strata in the eastern Ordos near the Yellow River (Figure 3), which closely overlaps with the ca. 40–30 Ma AFT dates from the eastern Ordos Block from transects 1 and 2 (Figure 8a and 8b). In the Xizhoushan of transect 3, published AFT dates range from 133–48 Ma, but the majority of dates are ca. 70–48 Ma (Figure 8c). In comparison, a new mean AHe date of ca. 35 Ma was collected from a basement sample in a tributary of the Hutuo River (Figure 4).

In the Hengshan and Wutaishan of transect 4, AFT and AHe dates tend to be > 50 Ma and generally increase in date with higher elevation or distance from the range-bounding fault (Figure 8d; Clinkscales et al., 2020). East of the Wutaishan in the Taihangshan (Figure 4), there is a wide range of AFT dates from ca. 110 to 15, but with a greater population cluster at ca. 60–30 Ma (Figure 8d) and sample elevations tend to be <~1,250 m. Mean AHe dates from the Taihangshan range from 50 to 15 Ma with a single grain date as young as ca. 12 Ma. In comparison, mean ZHe dates from the Taihangshan range from 80 to 70 Ma with a single grain date as young as ca. 60 Ma (Chang et al., 2019). In the Wutaishan and Taihangshan, ZHe, and ZFT dates also tend to be > 300 Ma (Clinkscales et al., 2020; Qing et al., 2008), significantly older than the dates recorded from the other low-temperature thermochronometers in the region. These data are not shown in Figure 8d and these older cooling dates are interpreted to record exhumation prior to deposition of the lower Paleozoic strata (e.g., Clinkscales et al., 2020).

The compilation of the low-temperature thermochronologic data is presented relative to latitude and elevation across the Shanxi Rift (Figure 9a and 9b). AFT dates from the southern to northern rift segment generally cluster at a higher proportion between ca. 50 and 30 Ma (Figure 9c). However, the AFT dates >70 Ma are more often located in the north-central and northern rift zone; the exception are the AFT dates from the upper elevations of the Zhongtiaoshan (Figure 5d and 5e). There also does not appear to be a strong correlation between AFT date and elevation, although the highest elevations in the Shanxi Rift (e.g., Wutaishan) are associated with AFT dates of >130 Ma (Figure 9b; e.g., Clinkscales et al., 2020). New and previously published AHe dates are also widely distributed across latitude and elevation with the greatest number of single-grain dates between ca. 50 and 20 Ma (Figure 9c).

6. Inverse Modeling Results

Inverse modeling results include: (1) single-sample AFT inverse modeling results from the lower and upper elevation samples of four elevation transects from the Huashan, Zhongtiaoshan, and Huoshan, and (2) multi-sample elevation transect modeling results from the Huashan and Zhongtiaoshan.

6.1. Single-Sample AFT Inverse Modeling

Thermal history inversion results from the eastern Huashan elevation transect (HS-2) include the low elevation sample (HS-2-590) collected adjacent to the Huashan fault and an upper elevation sample (HS-2-1810). Both are characterized by unimodal track length distributions from >30 HCTLs (Figure 10a and 10b). The results for HS-2-590 are consistent with an episode of cooling from below the AFT PAZ (>~120 °C) by ca. 45–35 Ma, followed by a period of slow cooling at temperatures of <60 °C by ca. 30–20 Ma. A cooling event at this time is corroborated by a mean AHe date of 34 ± 7 Ma. However, the single grain AHe data of HS-2-590 exhibit a positive date-eU correlation—although the correlation is within a narrow eU range of ~20 ppm (Figure 7b)—implying that this sample may have experienced an episode of slow cooling within the AHe PRZ after ca. 35–30 Ma, as inferred from the AFT inversion results.

The AFT modeling results of HS-2-1810 show an episode of fast cooling into the AFT PAZ by ca. 50–45 Ma to temperatures <60ºC prior to ca. 30 Ma, followed by slow cooling until the present (Figure 10b). The AHe data for HS-2-1810 are characterized by dispersed single grain AHe dates (Table 3) that do not meet the criteria to report a mean AHe date, nor are they associated with a date-eU correlation. Inversion results for HS-2-1810 suggest that the sample experienced negligible cooling by Miocene time. These model results are consistent with the absence of AHe dates of < ca. 20 Ma.

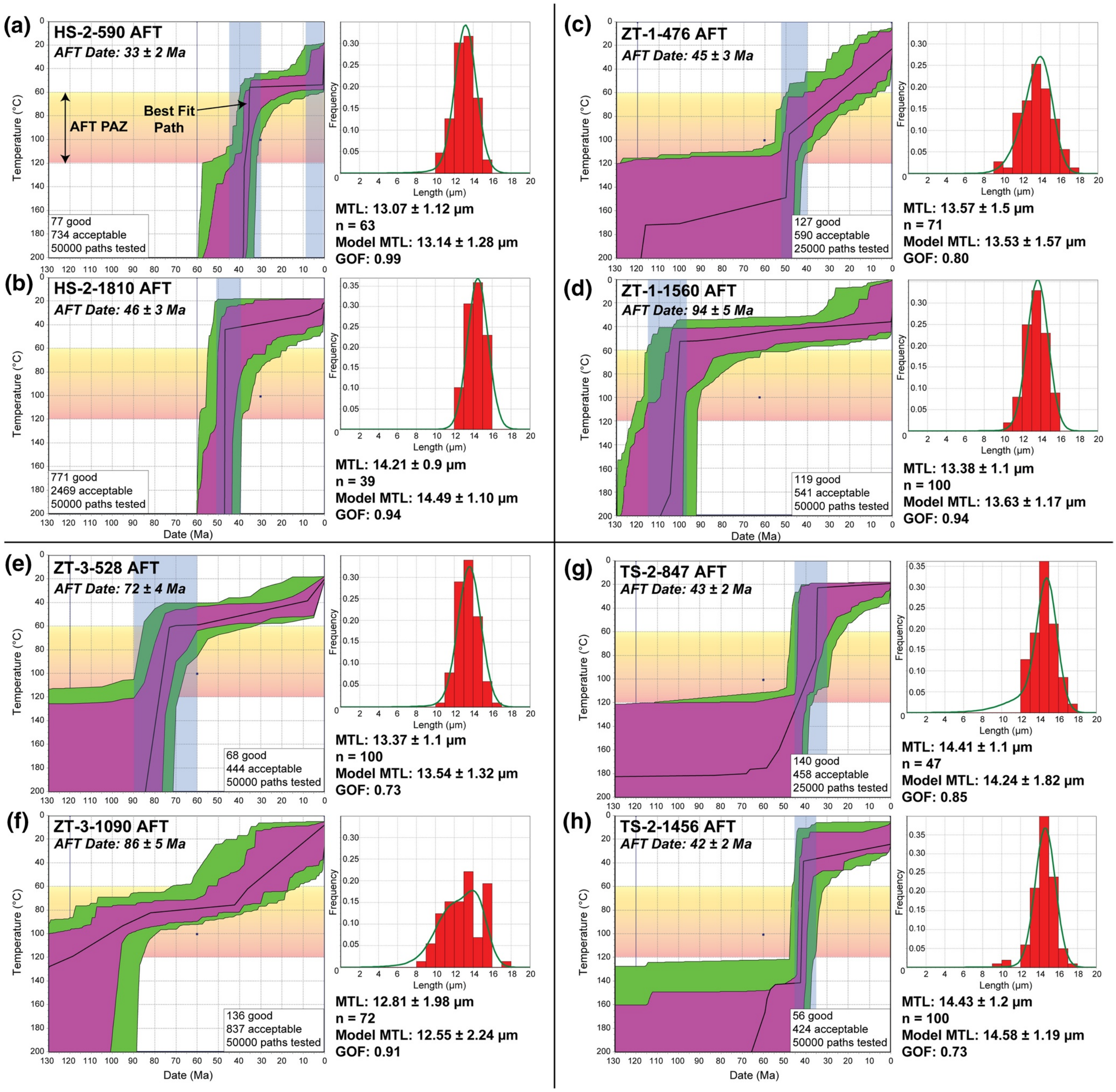

Figure 10. HeFTy inverse modeling results for the low elevation and an upper elevation sample from transects (a and b) HS-2, (C–D) ZT-1, (E–F) ZT-3, and (G–H) TS-2. Each transect includes: (left column) date versus temperature modeled envelopes showing the number of "good" and "acceptable" paths for 25,000 or 50,000 model runs; (right column) histogram with the measured mean track length (MTL) and the model MTL from the best fit path and its goodness of fit to the measured track length data (GOF; 1 = perfect fit).

Thermal history modeling results from the eastern Zhongtiaoshan transect (ZT-1) include the low elevation sample (ZT-1-476) collected adjacent to the Zhongtiaoshan fault and an upper elevation sample (ZT-1-1560). ZT-1-476 yielded an AFT date of 45 ± 3 Ma and shows a unimodal to mixed track length distribution (Figure 10c); in comparison, ZT-1-1560 yielded an AFT date of 94 ± 5 Ma and a unimodal track length distribution (Figure 10d). The inversion results from ZT-1-476 show an episode of cooling into the AFT PAZ by ca. 50 Ma followed by a monotonic cooling trend to the present. This sample may have experienced protracted cooling within the AHe PRZ by ca. 30 Ma, as inferred from the dispersed AHe single grain dates (Table 3), although a positive date-eU correlation is not clearly observed (Figure 7c). However, the AHe data from ZT-1-476 do suggest that cooling to temperatures <~40°C occurred by ca. 24 Ma, corresponding with the youngest single grain AHe date.

Modeling results for ZT-1-1560 invoke fast cooling through the AFT PRZ from ca. 115 to 100 Ma. After 90–80 Ma, the sample likely resided at temperatures <~60 ºC. These inversion results are corroborated by the AHe mean date of 111 ± 10 Ma, which together suggest that this upper elevation sample preserves a pronounced cooling event by ca. 115–100 Ma not recorded from the AFT and AHe thermochronometers in the lower elevations. Based on modeling results from ZT-1-476 and ZT-1-1560, this transect records at least two discrete cooling events at ca. 115–100 Ma and by ca. 50–40 Ma, but with minor amounts of cooling since the Miocene. We further tested these results by modeling the full elevation transect using QTQt described below in Section 6.2.

Thermal history modeling from the western Zhongtiaoshan transect (ZT-3) include the low elevation sample (ZT-3-528) collected near the Zhongtiaoshan fault and an upper elevation sample (ZT-3-1090). We do not present modeling results for the highest elevation sample of this transect (ZT-3-1346) because it did not contain sufficient HCTLs (Table 2). ZT-3-528 has an AFT date of 72 ± 4 Ma with a unimodal length distribution (Figure 10e). The modeling results from ZT-3-528 suggest that cooling into the AFT PAZ occurred by ca. 90–85 Ma, followed by slow cooling above the PAZ after ca. 60 until the present. Latest cooling may have occurred sometime in the Neogene, but the exact timing is unconstrained by our data. AHe dates from ZT-3-528 show significant intrasample date dispersion with a well-defined positive date-eU correlation (Figure 7e); these data strongly support slow and prolonged cooling within the AHe PRZ. The youngest single grain date of ca. 15 Ma from ZT-3-528 suggests that this sample cooled to temperatures of <~40°C by the Miocene.

ZT-3-1090 yielded an AFT date of 86 ± 5 Ma and a mixed track length distribution (Figure 10f). ZT-3-1090 AFT modeling results suggest that cooling into the PAZ most likely occurred by as late as 100 Ma, followed by slow cooling rates within the PAZ and an increase in cooling rates after ca. 50–40 Ma (Figure 10f). The prolonged cooling in the PAZ is supported by the mixed length track distribution. The single grain dates from ZT-3-1090 tend to be dispersed and show a positive date-eU correlation, although the eU values are within a narrow 15 ppm range (Table 3; Figure 7e). This dispersion is likely a result of slow or protracted cooling within the AHe PRZ. In contrast to the AFT inversion results, the youngest single grain AHe date of ca. 55 Ma suggests that this sample may have cooled to temperatures of <~40°C by this time. In either case, there appears to be negligible cooling since the Miocene. When the inversion models from ZT-3-528 and ZT-3-1090 are considered together, the results indicate that cooling into the PAZ occurred across the elevation transect by as late as ca. 80–70 Ma with Miocene to present cooling initiating from temperatures <~40 °C.

Two thermal history modeling results are shown for the Huoshan (TS-2). Samples TS-2-847 and TS-2-1456 are, respectively, the lowest and highest elevation samples from this transect and yielded AFT dates of 43 ± 2 Ma and 42 ± 2 Ma. Both are characterized by unimodal track length distributions and long mean track lengths of 14.4 μm, indicative of fast cooling at the time of the AFT dates (Figure 10g and 10h). This is supported by modeling results, which indicate an episode of pronounced cooling through the AFT PAZ beginning ca. 45 Ma until ca. 40–30 Ma and predict that after ca. 30 Ma, these samples resided at temperatures <~40°C–50°C. A mean AHe date of ca. 21 Ma for TS-2-1456 suggests that cooling through the AHe PRZ likely occurred by this time. Additionally, the youngest single grain AHe date of ca. 18 Ma further supports cooling to temperatures of <~40°C by the Miocene.

6.2. Multi-Sample Elevation Transect Inverse Modeling

Elevation transect inverse modeling results from QTQt are presented for the eastern Huashan (HS-2) and western Zhongtiaoshan (ZT-1) transects (Figure 11). The expected (maximum likelihood) t-T paths for the HS-2 transect predict a rapid cooling event beginning ca. 50–45 Ma and ending by ca. 35 Ma, at which time all samples cooled through the AFT PAZ at a rate of ~16°C/Ma (Figure 11a). After ca. 35 Ma, these samples resided at temperatures <60°C. The model invokes slight reheating, but this reheating event is likely negligible or a modeling artifact. The mean AHe dates from the HS-2 transect are consistently > ca. 30 Ma and tend to show no correlation between date and eU, except HS-2-590, the lowest elevation sample. This suggests that HS-2-590 may have resided for some period in the AHe PRZ. Most importantly, the modeling results

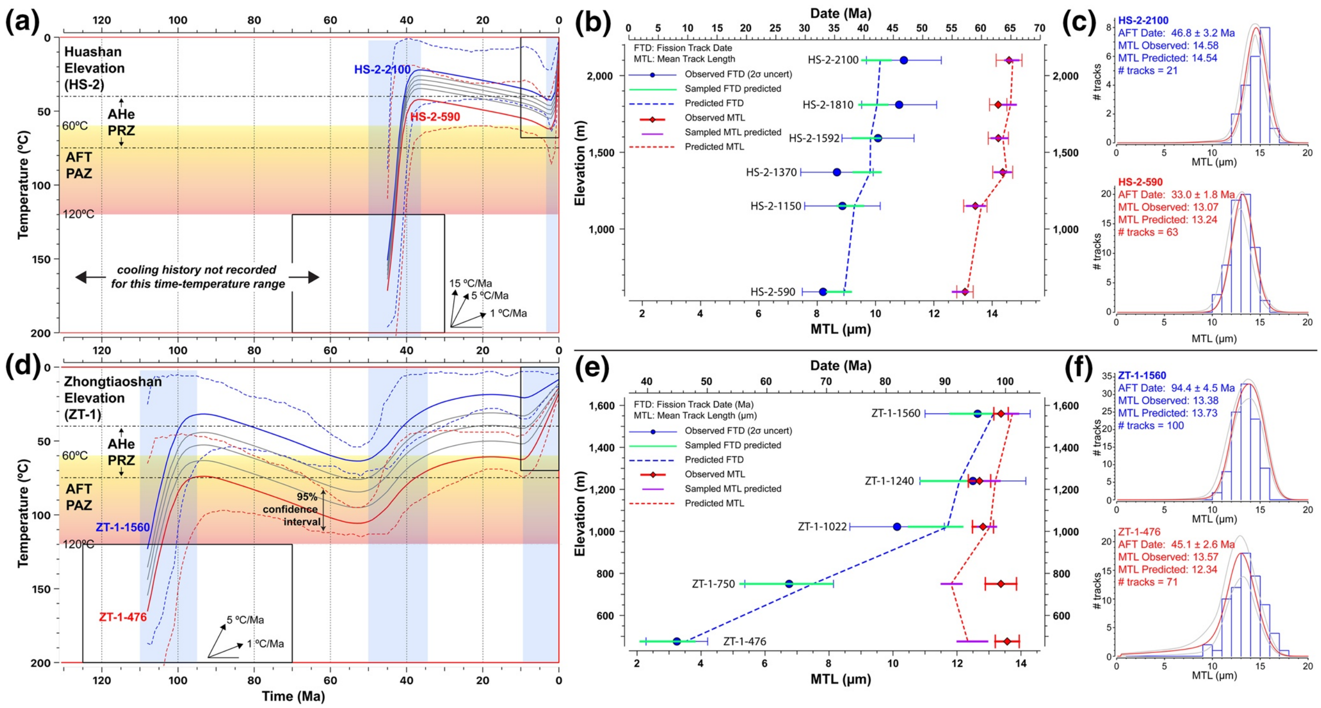

Figure 11. QTQt elevation transect AFT inverse modeling results from the (a) HS-2 and (b) ZT-1 transects. Each transect includes: (left column) time versus temperature modeling results, highlighting the expected (most likely) tT-path for the lowest elevation sample in red and upper elevation sample in blue; (center column) modeling predictions versus the measured AFT date and MTL data; (right column) track length distribution and track length model fit. AFT, apatite fission track; MTL, mean track length.

indicate that all samples in the HS-2 transect were in the upper ~2 km of the crust prior to the late Miocene. Observed versus predicted fission track dates and mean track lengths show a good fit and an increase in the predicted fission track date and mean track length with increasing elevation (Figure 11b and 11c).

The expected t-T paths for ZT-1 predict two main cooling episodes prior to the Neogene: (1) a ca. 110–95 Ma event associated with a cooling rate of ~7.5°C/Ma; and (2) a ca. 50–35 Ma event at a rate of ~2.0 °C/Ma (Figure 11d). In contrast with the single-sample HeFTy modeling (Figure 10c and 10d), the multi-sample QTQt elevation model produces a unified solution which accounts for the ca. 110 Ma cooling event recorded in the uppermost elevation sample (ZT-1-1560) and the ca. 50–45 Ma event recorded by the lowest elevation sample (ZT-1-476). The intermediary reheating event at ca. 95–50 Ma is likely a modeling artifact to better fit the track length distributions. The results suggest that cooling at ca. 110–95 Ma placed the lowermost samples within the AFT PAZ until after ca. 30 Ma when samples cooled to temperatures of <~60°C–65°C prior to cooling predicted to commence by the late Miocene. The two lowermost samples show a mismatch between the observed (ZT-1-476: 13.6 μm) and the predicted (ZT-1-476: 12.3 μm) mean track lengths for the expected t-T path (Figure 11e and 11f), suggesting that the model overpredicts the magnitude of annealing and that the lower elevation samples may have resided within the AFT PAZ for less time than predicted by the modeling. However, ZT-1-476 and ZT-1-750 have <100 confined track length measurements (see Table 2), so the observed track length distribution may not fully represent the thermal history of these samples.

7. Timing of Cooling Events

Low-temperature thermochronometric data and thermal history models from the Shanxi Rift, eastern Ordos block, and Taihangshan reveal Mesozoic-Cenozoic cooling events during the: (1) Middle Jurassic–earliest Cretaceous, ca. 160–135 Ma; (2) Early Cretaceous–Late Cretaceous, with discrete cooling events between ca. 120 Ma to ca. 70 Ma; (3) Eocene–early Oligocene, ca. 50–30 Ma; (4) Oligocene, ca. 25–20 Ma; and (4) Miocene-Recent, post ca. 10 Ma (Figures 12a–12c). An earlier episode of exhumation is recorded from ZHe and ZFT data in the Wutaishan, where ZHe and ZFT dates from basement rocks are commonly >500 Ma

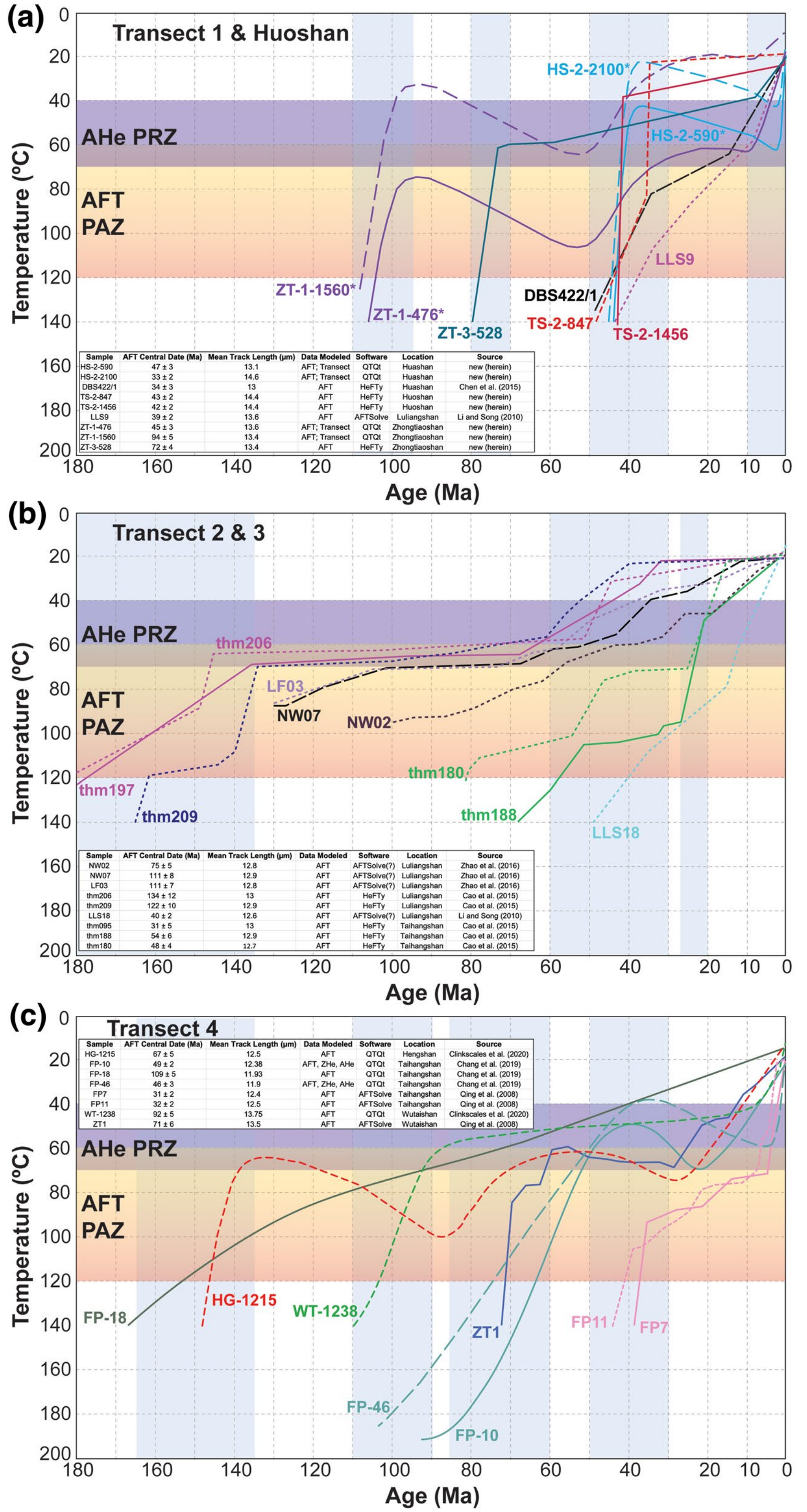

Sample	AFT Central Date (Ma)	Mean Track Length (μm)	Data Modeled	Software	Location	Source
HS-2-590	47 ± 3	13.1	AFT; Transect	QTQt	Huashan	new (herein)
HS-2-2100	33 ± 2	14.6	AFT; Transect	QTQt	Huashan	new (herein)
DBS422/1	34 ± 3	13	AFT	HeFTy	Huashan	Chen et al. (2015)
TS-2-847	43 ± 2	14.4	AFT	HeFTy	Huoshan	new (herein)
TS-2-1456	42 ± 2	14.4	AFT	HeFTy	Huoshan	new (herein)
LLS9	39 ± 2	13.6	AFT	AFTSolve	Luliangshan	Li and Song (2010)
ZT-1-476	45 ± 3	13.6	AFT; Transect	QTQt	Zhongtiaoshan	new (herein)
ZT-1-1560	94 ± 5	13.4	AFT; Transect	QTQt	Zhongtiaoshan	new (herein)
ZT-3-528	72 ± 4	13.4	AFT	HeFTy	Zhongtiaoshan	new (herein)

Sample	AFT Central Date (Ma)	Mean Track Length (μm)	Data Modeled	Software	Location	Source
NW02	75 ± 5	12.8	AFT	AFTSolve(?)	Luliangshan	Zhao et al. (2016)
NW07	111 ± 8	12.9	AFT	AFTSolve(?)	Luliangshan	Zhao et al. (2016)
LF03	111 ± 7	12.8	AFT	AFTSolve(?)	Luliangshan	Zhao et al. (2016)
thm206	134 ± 12	13	AFT	HeFTy	Luliangshan	Cao et al. (2015)
thm209	122 ± 10	12.9	AFT	HeFTy	Luliangshan	Cao et al. (2015)
LLS18	40 ± 2	12.6	AFT	AFTSolve(?)	Luliangshan	Li and Song (2010)
thm095	31 ± 5	13	AFT	HeFTy	Taihangshan	Cao et al. (2015)
thm188	54 ± 6	12.9	AFT	HeFTy	Taihangshan	Cao et al. (2015)
thm180	48 ± 4	12.7	AFT	HeFTy	Taihangshan	Cao et al. (2015)

Sample	AFT Central Date (Ma)	Mean Track Length (μm)	Data Modeled	Software	Location	Source
HG-1215	67 ± 5	12.5	AFT	QTQt	Hengshan	Clinkscales et al. (2020)
FP-10	49 ± 2	12.38	AFT, ZHe, AHe	QTQt	Taihangshan	Chang et al. (2019)
FP-18	109 ± 5	11.93	AFT	QTQt	Taihangshan	Chang et al. (2019)
FP-46	46 ± 3	11.9	AFT, ZHe, AHe	QTQt	Taihangshan	Chang et al. (2019)
FP7	31 ± 2	12.4	AFT	AFTSolve	Taihangshan	Qing et al. (2008)
FP11	32 ± 2	12.5	AFT	AFTSolve	Taihangshan	Qing et al. (2008)
WT-1238	92 ± 5	13.75	AFT	QTQt	Wutaishan	Clinkscales et al. (2020)
ZT1	71 ± 6	13.5	AFT	AFTSolve	Wutaishan	Qing et al. (2008)

Figure 12. Compilation of published and new tT-paths across the four transects shown in Figures 3 and 4. Each tT-path represents a single best-fit (HeFTy) or expected (QTQt) path output from a published inversion model and does not portray the range of uncertainty/permissible tT-paths associated with each model. The inversion model outputs are primarily from AFT data, except if noted otherwise. Refer to the tables for additional information for each of the depicted paths, including the "Software" utilized in the modeling process. AFT, apatite fission track.

(Clinkscales et al., 2020; Qing et al., 2008).These dates are interpreted to record exhumation associated with the development of a regional unconformity above basement and Proterozoic metasedimentary rocks and prior to the deposition of the overlying Paleozoic-Mesozoic stratigraphic section (Clinkscales et al., 2020).

The low-temperature record of cooling during the ca. 160–135 Ma Yanshanian orogeny appears restricted to the Lüliangshan and Hengshan (Figures 4, 12b, and 12c; Cao et al., 2015; Clinkscales et al., 2020). Samples recording the Yanshanian cooling event in the northern Lüliangshan are from Neoarchean–Paleoproterozoic basement rocks primarily located in the core of a basement-involved anticline, which differ significantly from AFT dates of ca. 75–70 Ma from Triassic-Jurassic strata in an adjacent syncline (Figure 4). These Late Cretaceous dates indicate that the Jurassic strata in the Lüliangshan were sufficiently buried to reset the AFT dates in detrital apatite grains, possibly due to Early Cretaceous sediment burial (J. Zhao et al., 2016). We postulate that a Cretaceous sedimentary section—corelative to the Lower Cretaceous strata of the Ordos block which unconformably overlies the Paleozoic-Jurassic strata—buried the Triassic–Jurassic section in the Lüliangshan and reset the detrital apatite, but did not sufficiently bury the adjacent anticline to reset the basement samples (Figure 4).

The second principal cooling event which commenced as early as ca. 120–110 Ma is recognized across all four transects of the Shanxi Rift (Figures 12a–12c). Cooling at this time postdates a magmatic event at ca. 140–130 Ma by >~20 Myr, and thus, is not related to post-magmatic thermal relaxation. Our new thermal history models from the Zhongtiaoshan suggest that cooling commenced in the south by ca. 110–100 Ma (Figures 10f and 11d), but mid-temperature thermochronometers from the Huashan indicate that cooling may have initiated even earlier, by ca. 120 Ma. For example, a biotite $^{40}Ar/^{39}Ar$ date of ca. 118 Ma was obtained from a ca. 142 Ma pluton in the eastern Huashan (Y.-T. Wang et al., 2019) and a K/Ar date of ca. 114 Ma from a ca. 127 Ma diorite pluton in the western Huashan (J. Zhang & Zheng, 1999). Also, sericite K/Ar dates from shear zone rocks adjacent to the Huashan fault cluster at ca. 120–107 Ma with a single date as young as ca. 85 Ma (J. Zhang & Zheng, 1999). In the northern rift, for comparison, previously published AFT thermal history models support cooling at ca. 110–65 Ma (Figure 12c; Clinkscales et al., 2020). And in the northern Taihangshan, ZHe dates indicate that cooling was underway by ca. 110–60 Ma (Figure 6e), overlapping with the onset of cooling at ca. 95–90 Ma (e.g., FP-10 in Figure 12c; Chang et al., 2019). Moreover, cooling in the southeastern Ordos block was underway by 94–60 Ma, as indicated by ZFT dates from exhumed Paleozoic-Triassic strata (Figure 3; X. Li & Song, 2010).

Our new thermal history modeling from the Huashan, Zhongtiaoshan, and Huoshan is consistent with a third cooling event between ca. 50 and 30 Ma (Figures 10–12a) and the compilation of new and previously published data show the highest density of AFT and AHe dates centered at ca. 38 Ma across the region (Figure 9). Rapid cooling at this time is clearly observed in the Huashan and Huoshan, where there is a narrow range of AFT dates across the elevation transects and some overlapping mean AHe dates (Figures 5a, 5b, and 6). In the Huoshan, for example, there is no discrete correlation between date and elevation (Figure 6). All samples from the Huoshan are located below the Dianziliang planation surface, interpreted to be preserved in the upper elevations of the Huoshan (see Figure 2 in Xiong et al., 2018). We suspect that the Eocene-Oligocene cooling event led to the development of this planation surface (Figure 13; e.g., K. Zhang, 2008).

In the central Lüliangshan, the mean AHe dates of ca. 33–29 Ma from Triassic-Jurassic sandstone samples (CLS; Figure 3) suggest: (1) that this upper Mesozoic stratigraphic section was sufficiently buried to reset the detrital apatite grains, and (2) that an Eocene–Oligocene cooling event likely contributed to the erosion of the missing overlying stratigraphic section. These AHe dates from the Lüliangshan overlap with some AFT dates from the central and northern Lüliangshan (Figures 8b–8c) and a modeled cooling event at ca. 60–30 Ma (Figure 12b).

Cooling at ca. 25–20 Ma in the Taihangshan is recorded from AFT and mean AHe dates at elevations of <1,000 m (e.g., Chang et al., 2019; J. S. Zhang et al., 2002; Figure 8b and 8d) and by thermal history models (thm180/thm188 in Figure 12b; Cao et al., 2015). However, this cooling event is not widely distributed across the Shanxi Rift or Taihangshan and appears to be restricted to the lowest elevation of the Taihangshan and near Eastern Taihangshan fault, suggesting this fault may have been active at this time. Cooling

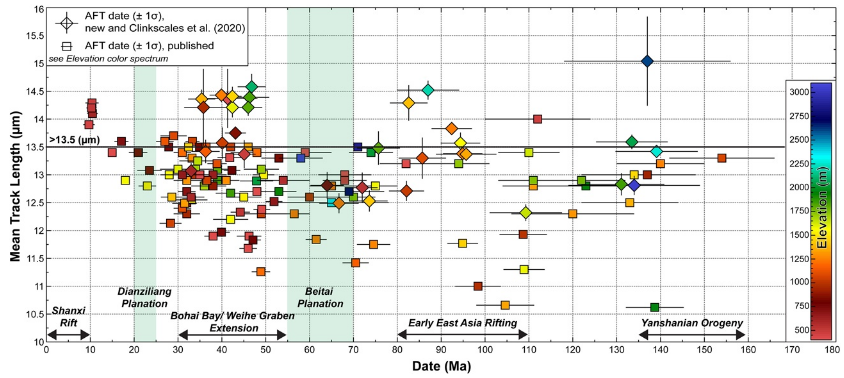

Figure 13. Date versus mean track length "boomerang" plot of published and new AFT data. New AFT data is grouped with previously published AFT data from Clinkscales et al. (2020). Symbols are color coded based on sample elevation. Interpreted ages of the Beitai and Dianziliang planation surfaces shown in green. Major tectonic events indicated above the *x*-axis.

at this time also overlaps with the eruption of Oligocene–Miocene basalts in the northern Shanxi Rift (see Section 2.2.3), but how these coeval events may be related is uncertain.

The regional compilation of AHe and AFT data suggest that localities characterized by thermochronologic dates <10 Ma are rare (Figure 9). A notable exception is in the northwestern Huashan, where low elevation samples yielded AFT dates of ca. 10 Ma with mean track lengths of ∼14–14.5 μm (Figure 8a). These mean track lengths, however, are based on a statistically small number of confined track lengths (≤20; J. Liu et al., 2013). In comparison, our new data from a nearby transect in the northwestern Huashan (HS-1) yielded AFT dates of >35 Ma and dispersed single grain AHe dates of ca. 5, 10, and 23 Ma (Figure 5a), and new AHe and AFT dates from the northeastern Huashan (HS-2) yielded dates of >20 Ma (Figure 5b). Therefore, we argue that northern Huashan, between transects HS-1 and HS-2 (Figure 3), likely shares a similar cooling history characterized by Miocene and younger cooling from temperatures <∼60°C–70°C, in contrast to rapid cooling from temperatures >120°C (J. Liu et al., 2013).

8. Overview of Regional Tectonic and Structural Evolution

8.1. Jurassic-Late Cretaceous

The Middle Jurassic-Early Cretaceous Yanshanian orogeny resulted in shortening across much of North China (e.g., Zhang et al., 2014) and the formation of basement-involved folds in the northern Shanxi Rift (Clinkscales & Kapp, 2019). The low-temperature thermochronology from the northern Lüliangshan (Cao et al., 2015) and Hengshan (Clinkscales et al., 2020) helps bracket the timing of this orogenic event. By ca. 135 Ma, the subducting Izanagi (i.e., paleo-Pacific) oceanic slab began to rollback under North China (e.g., S. Liu, Gurnis, et al., 2017), following a period of flat-slab subduction during the Yanshanian orogeny, leading to the reestablishment of an asthenosphere (mantle) wedge between the Izanagi plate and the continental lithosphere of North China (e.g., J. Liu et al., 2019). Convection in the asthenosphere may have resulted in the thermal "erosion" (He, 2014) or delamination (e.g., Lin & Wei, 2018) of the overlying continental lithosphere. The lithosphere appears to have been thinned on the order of >∼100 km east of the Taihangshan and the Daxin'anling-Taihangshan gravity lineament (e.g., Menzies et al., 2007) (Figure 1b). Slab rollback accompanied extension and fault reactivation in the middle to upper crust, including the development of extensional "core complex" structures from ca. 130 to 100 Ma (Figure 14a; e.g., Davis et al., 2001; J. H. Yang et al., 2007) and left-lateral reactivation of the Tanlu fault and conjugate right-lateral shear along the northern margin of the Dabieshan (Grimmer et al., 2002; Ratschbacher et al., 2003, 2000). The western segment of the Qinling fault may also have been active at this time, as suggested by exhumation at ca. 120–100 Ma in the northern Qinlingshan (Heberer et al., 2014). Early-Late Cretaceous extension led to the formation of backarc basins along the eastern Asian margin, including the Gyeongsang Basin in the Korean Peninsula (e.g., Cheon et al., 2020) and in eastern South China (e.g., J. Li et al., 2014) (Figure 14a).

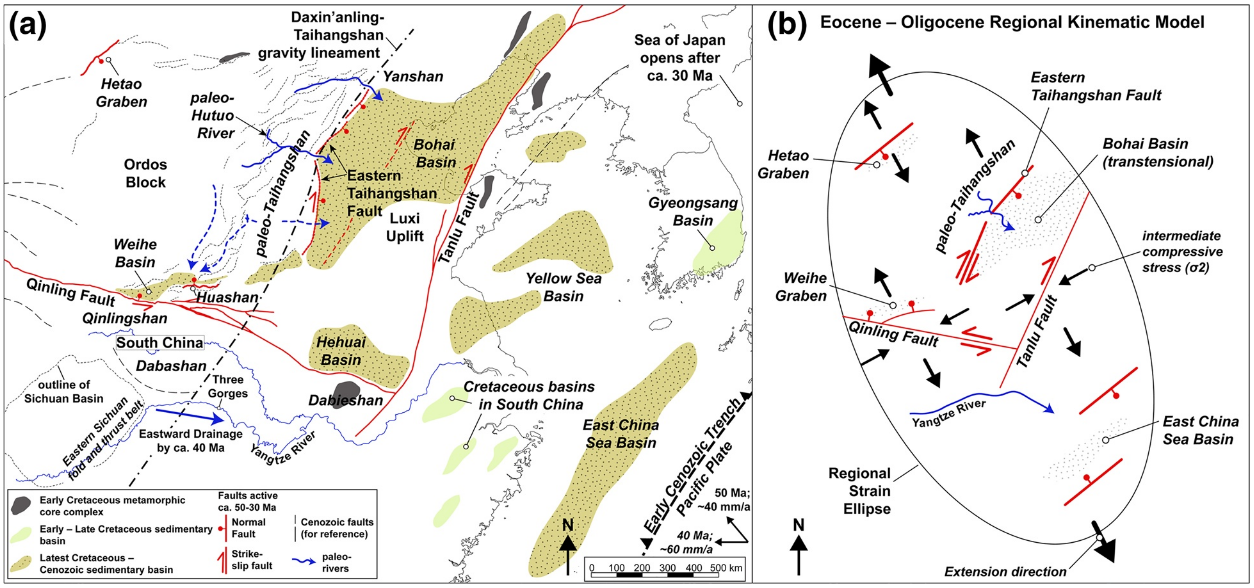

Figure 14. (a) Regional map of North China and northern South China showing the Eastern Taihangshan, Tanlu, and Qinling faults, select Early Cretaceous "metamorphic core complexes," and generalized locations of Early–Late Cretaceous basins, including the Gyeongsang Basin in the Korean Peninsula (see text for sources). The range-bounding faults of the circum-Ordos rifts shown by thin dashed black lines. Rivers (blue lines) illustrate the erosional denudation of the paleo-Taihangshan highlands. Approximate location of the Early Cenozoic trench to the southeast with Pacific plate trajectories and velocities after Müller et al. (2019). (b) Kinematic model of North China and East China Sea during the Eocene–Oligocene. Modified after Shi et al. (2020) to include the Eastern Taihangshan fault, concurrent right-lateral slip along the Tanlu fault, and extension in the East China Sea. Strain ellipse illustrates a regional NW-SE extensional environment resulting in coeval slip along the Eastern Taihangshan, Qinling, and Tanlu faults.

Based on the thermal history modeling from the Zhongtiaoshan, Hengshan, and Wutaishan (Clinkscales et al., 2020), basement rocks cooled at least ∼50°C–60°C by the Early-Late Cretaceous, equating to ∼2–2.5 km of erosion (assuming a 25°C/km geothermal gradient). This may have led to the formation of the Beitai planation surface (e.g., Cao et al., 2015). Exhumation of the Ordos Block also commenced by ca. 100 Ma (e.g., Xiao et al., 2005), including in its southeastern margin, as indicated by ZFT dates of ca. 94–60 Ma (Figure 8a). Therefore, the Ordos Basin had transformed from an internally drained depocenter during the Yanshanian orogeny (e.g., Ritts et al., 2009) to an incised basin and region of net erosion by the Late Cretaceous. The mechanism controlling exhumation at this time is uncertain, but one potential explanation may be the early development of the Eastern Taihangshan fault (e.g., Chang et al., 2019; Clinkscales et al., 2020). However, this interpretation is problematic because the oldest syn-rift deposits in the western Bohai Basin are thought to be early Eocene or Paleocene in age (e.g., Allen et al., 1997). Alternatively, exhumation in the Shanxi Rift and eastern Ordos Block may have been a result of widespread erosional denudation resulting from a decrease in base level as a response to regional extension, which accompanied the formation of Cretaceous metamorphic core complexes and backarc basins (Figure 14a). In the region of the Shanxi Rift, slow cooling rates persisted after ca. 80–70 Ma until ca. 50 Ma.

8.2. Eocene-Oligocene

Cooling during the Eocene-Oligocene (ca. 50–30 Ma) overlaps with the deposition of Paleogene syn-rift deposits in the Bohai Basin. The Bohai Basin is one of several extensional basins which formed along the eastern margin of Asia during the Late Cretaceous-Paleogene (Figure 14a). The onset of extension coincided with the subduction of the Izanagi-Pacific oceanic spreading center and the transition between Izanagi to Pacific oceanic plate subduction under the eastern margin of Asia by ca. 60–55 Ma (e.g., S. Liu et al., 2017; X. Liu et al., 2017; Seton et al., 2015; Wu & Wu, 2019), as well as a decrease in convergence rates between the Pacific and Eurasian plates (Northrup et al., 1995). The Bohai Basin is a rhomboid-shaped transtensional basin with a modern-day width of ∼400–450 km in its center, defined by the Eastern Taihangshan and Tanlu faults bounding the western and eastern margins (Allen et al., 1997; F. Yu & Koyi, 2016), and is estimated to have experienced a minimum of ∼30% extension during rifting (Hellinger et al., 1985). Two-dimensional seismic profiles from the western margin indicate that the Eastern Taihangshan fault projects to a depth of >10 km and offsets prerift Cretaceous and older bedrock and a basal Paleogene unconformity to a depth of ∼8–10 km (Qi & Yang, 2010) (Figure 14b). The upper Paleocene-Oligocene section consists of ∼2–8 km of synextensional sedimentary deposits truncated by an unconformity and overlain by ∼1–3 km of postrift Neogene-Quaternary clastic sedimentary rocks (Qi & Yang, 2010). The unconformity bounding the top of the syn-rift section is late Oligocene in age and has been attributed to a brief period of shortening and basin inversion between the main phase of rifting in the Bohai Basin and subsequent Neogene thermal subsidence (Allen et al., 1997). The synextensional basin fill is dominated by nonmarine alluvial, braided fluvial, and deltaic-lacustrine clastic rocks, sourced by paleo-river systems from the Taihangshan in the western margin of the basin (e.g., H. Chen et al., 2020). One such example is the paleo-Hutuo River. This river bisects the frontal escarpment of the Xizhoushan (Figure 4) and AHe data from a bedrock sample in one of its tributaries yielded a date of ca. 35 ± 5 Ma, potentially recording canyon incision and river integration at that time. In the central and northern rift, cooling is interpreted to represent the erosional denudation of the paleo-Taihangshan highlands, which formed in the western footwall of the Eastern Taihangshan fault (Figure 14a). By the late Eocene, drainage systems across eastern Asia flowed east into the opening rift basins, as suggested the paleo-rivers that bisected the paleo-Taihangshan, and by the Yangtze River in South China, interpreted to have been redirected eastward by ca. 40 Ma (e.g., Richardson et al., 2008).

Eocene-Oligocene cooling also occurred contemporaneously with the opening of the Weihe Graben and is recorded by low-temperature thermochronometers across much of the northern Qinlingshan (e.g., Z. Yang et al., 2017, Figure 3). In the Huashan, the rapid cooling event beginning ca. 50–40 Ma and ending by ca. 30 Ma is likely associated with footwall uplift and denudation along the flanks of the Weihe Graben and displacement across the Huashan fault (e.g., Mercier et al., 2013; Shi et al., 2020). A similar cooling signature is observed in the Huoshan to the north, but the adjacent Linfen Basin has no recognized Eocene-Oligocene sedimentary record, so displacement along the Huoshan fault at the time is difficult to ascertain. Cooling in the Huoshan may be a result of high rates of erosion which supplied sediment to the Weihe Graben to the south and/or the Bohai Basin to the east.

Finally, the Shanxi Rift and Taihangshan region is contextualized within a linked kinematic framework for Eocene–Oligocene deformation in North China and the eastern Asian margin. Fault offset at this time occurred contemporaneous along the NNE–striking Eastern Taihangshan and Tanlu faults and the ∼E–striking Qinling and Huashan faults (Mercier et al., 2013; Shi et al., 2019, 2020; Y. Zhang et al., 1999). This coeval deformation is thought to be a result of regional NW-SE extension, which reactivated the Eastern Taihangshan and Tanlu faults as right-lateral faults and the Qinling fault as left-lateral oblique-slip structure (e.g., Y. Zhang et al., 2003) (Figure 14b). However, the Qinling and Huashan faults may have been intermittently characterized by right-lateral slip due to NE-SW extension (Mercier et al., 2013). For our purposes, it is noteworthy that concurrent deformation occurred along these nearly orthogonal fault systems, and oblique-slip reactivation prompted the opening of the Bohai Basin and the Weihe Graben. The reactivation of the Qinling fault may be further evidence of far-field strain effect associated with India-Asia collisional orogenesis during the Eocene (e.g., H. Chen et al., 2015; S. Hu et al., 2006), which occurred synchronously with backarc extension in eastern Asia (e.g., A. Yin, 2010). If correct, this would represent an early stage of far-field strain related to the Himalayan-Tibetan orogen which predates Miocene east-directed strike-slip propagation (e.g., Duvall et al., 2013) and attendant extension north of the Qinling fault (e.g., Tapponnier & Molnar, 1977).

8.3. Miocene-Quaternary Rifting

The low-temperature thermochronologic data and inversion modeling presented here, in combination with previous thermochronologic studies (e.g., Cao et al., 2015; Chang et al., 2019; Clinkscales et al., 2020; Webb, 2007; J. Zhao et al., 2016), indicate that the bulk of exhumation in the region largely predated Miocene and younger rifting. Although the modern landscape is distinctly defined by fault blocks and basins associated with latest extension (Figure 2), the magnitude of exhumation associated with this rifting event appears to be comparatively minor compared to the preceding Cretaceous and Eocene-Oligocene events. Uplifted fault blocks across the rift were exhumed from temperatures less than ∼70°C since the late Miocene and early Pliocene. This explains why late Miocene and younger AHe dates are rare throughout the rift zone. The magnitude of Miocene to present cooling in the Shanxi Rift also resembles that of the Baikal Rift, an analogous sigmoid-shaped intracratonic rift system in the interior of Asia with a Miocene and younger history of extension (Figure 1a; e.g., Petit & Déverchère, 2006). AFT dates from the Baikal Rift are predominantly Mesozoic or early Cenozoic and thermal history inversion results invoke cooling from <70°C–80°C starting in the latest Miocene and early Pliocene, following earlier cooling events during the Middle Jurassic-Early Cretaceous and latest Cretaceous-Paleocene (Jolivet et al., 2009). Latest cooling in the Baikal Rift suggests ≤~3 km of footwall uplift (assuming a ~25°C–30°C/km geothermal gradient). Other mountain belts in the interior of Asia (e.g., Altai Mountains; Figure 1a), show a similarly low magnitude (<~50°C) of Neogene cooling following earlier Mesozoic cooling events (e.g., Jolivet et al., 2007; Pullen et al., 2020). Although it is beyond the scope of this paper, we note that the late Cenozoic cooling histories for the extensive region north and northeast of the Tibetan Plateau appears to be characterized by relatively minor Cenozoic cooling and exhumation, allowing for the preservation of Mesozoic planation surfaces.

In the northern Shanxi Rift, metamict zircons yielded ZHe dates of ca. 13–8 Ma (Clinkscales et al., 2020), highlighting the importance of utilizing low-temperature thermochronometric techniques which may have closure temperatures <~60°C to precisely constrain the initiation of rift-related exhumation. Based on the lack of late Miocene and younger AHe dates in the presented data, the maximum Miocene and younger vertical footwall uplift on range-bounding faults is likely ≤~2 km across the rift zone, assuming a modern gradient of ~26°C/km and average surface temperatures of ~15°C–20°C. This may equate to fault throws of ~4–5 km assuming a footwall uplift to basin subsidence ratio of ~1:1–2.5 (i.e., 1 m of footwall uplift to 1–2.5 m of basin subsidence; e.g., de Gelder et al., 2019; Stein et al., 1988). Clinkscales et al. (2020) argued for ≤~2.5 km of fault throw in the northern Shanxi Rift, but we revise this estimate to a fault throw magnitude on the order of ~4–5 km accompanying ~2 km of footwall uplift and ~1.8 km of basin subsidence based on the thickness of syn-rift sedimentary rocks in the Hunyuan basin north of the Hengshan (Figure 4). Quaternary fault throw rates of >~0.7 mm/a in the northern rift (e.g., Middleton et al., 2017) would equate to ~5.6 km of fault throw if the rift initiated at ca. 8 Ma. Therefore, the Quaternary fault throw rates may be slightly higher than the long-term average, but are not considerably higher when considering the footwall uplift to basin subsidence ratios noted above. Footwall uplift and by inference, total displacement magnitudes, may be further tested by collecting low-temperature thermochronometric data along-strike of the same fault blocks (e.g., Curry et al., 2016), and the timing of rift initiation may be more precisely constrained by utilizing emerging thermochronometric techniques, such as metamict ZHe dates, which may be associated with lower closure temperatures than the AHe system (e.g., Ault et al., 2019). Finally, we argue that the Shanxi Rift developed along the eastern margin of the Ordos Block and the axis of the pre-existing paleo-Taihangshan highlands (Figure 14a).

9. Conclusions

A compilation of new and published low-temperature thermochronologic data from the Shanxi Rift and Taihangshan reveals that the bulk of upper crustal exhumation experienced in the region occurred during the Early-Late Cretaceous, ca. 110–70 Ma, and Eocene-Oligocene, ca. 50–30 Ma. The low-temperature cooling record for the Middle Jurassic-Early Cretaceous Yanshanian orogeny appears to be restricted to the Lüliangshan and Hengshan of the northern rift zone. In contrast Cretaceous cooling, which occurred after the Yanshanian orogeny, is recognized from the southern and northern rift zone and in the eastern Ordos Block. We interpret cooling during the Cretaceous to be associated with widespread erosional denudation responding to a decrease in base level in eastern North China, coincident with a phase of regional extension and rollback of the Izanagi plate. By ca. 50–30 Ma, the central to northern Shanxi Rift was part of the paleo-Taihangshan highlands of western rift shoulder of the Bohai Basin. These paleo-highlands were bounded to the east by the Eastern Taihangshan fault, which formed a major structural boundary that overlaps with the Daxin'anling-Taihangshan gravity lineament. In the southern rift, ca. 50–30 Ma cooling may be associated with extensional uplift along the Huashan and Qinlingshan and opening of the Weihe Graben. The most recent cooling event related to Late Miocene to Recent extensional exhumation in the Shanxi Rift appears to have occurred from temperatures ≤~40°C–70°C and the timing of initial extension for the modern rift is not precisely constrained from the AHe and AFT thermochronometers applied in this study. However, these data do indicate that the magnitude of footwall uplift across most of the modern rift zone is on the order of ≤~2 km.

Data Availability Statement

Data Availability Statement: Data sets (new and published) are available in the supporting information. Data sets are also available on the Mendeley Data repository (doi.org/10.17632/7nwz7nrt7z.1) https://data.mendeley.com/datasets/7nwz7nrt7z/1.

Acknowledgments

The authors thank Lin Ding, Fulong Cai, and XiaoHui Liu from the Institute of Tibetan Plateau Research, Chinese Academy of the Sciences for their logistical support during our field work. We thank Barbara Carrapa, Peter Reiners, Uttam Chowdhury, Jordan Abell, and Simon Stickroth for their assistance with data and sample collection and analysis. This research was funded by National Science Foundation Office of International Science and Engineering grant #1545859.

References

Allen, M. B., Macdonald, D. I. M., Xun, Z., Vincent, S. J., & Brouet-Menzies, C. (1997). Early Cenozoic two-phase extension and late Cenozoic thermal subsidence and inversion of the Bohai Basin, northern China. *Marine and Petroleum Geology*, *14*(7–8), 951–972.

Ault, A. K., Gautheron, C., & King, G. E. (2019). Innovations in (U–Th)/He, fission track, and trapped charge thermochronometry with applications to earthquakes, weathering, surface-mantle connections, and the growth and decay of mountains. *Tectonics*, *38*(11), 3705–3739.

Bonvalot, S., Balmino, G., Briais, A., Kuhn, M., Peyrefitte, A., Vales, N., et al. (2012). *World gravity map*. Paris, France: Bureau Gravimetrique International (BGI), Map, CGMW-BGI-CNES728, IRD.

Bureau of Geology and Mineral Resources of Shaanxi Province (BGMRSNX). (1990). *Regional geology of Shaanxi province*. Beijing, China: Geological Publishing House.

Cao, X., Li, S., Xu, L., Guo, L., Liu, L., Zhao, S., et al. (2015). Mesozoic–Cenozoic evolution and mechanism of tectonic geomorphology in the central North China block: Constraint from apatite fission track thermochronology. *Journal of Asian Earth Sciences*, *114*, 41–53.

Chang, J., Qiu, N., Liu, S., Xu, Q., & Liu, N. (2019). Post-Triassic multiple exhumation of the Taihang Mountains revealed via low-T thermochronology: Implications for the paleo-geomorphologic reconstruction of the North China Craton. *Gondwana Research*, *68*, 34–49.

Chen, H., Hu, J., Wu, G., Shi, W., Geng, Y., & Qu, H. (2015). Apatite fission-track thermochronological constraints on the pattern of late Mesozoic–Cenozoic uplift and exhumation of the Qinling Orogen, central China. *Journal of Asian Earth Sciences*, *114*, 649–673.

Chen, H., Zhu, X., Wood, L. J., & Shi, R. (2020). Evolution of drainage, sediment-flux and fluvio-deltaic sedimentary systems response in hanging wall depocentres in evolving non-marine rift basins: Paleogene of Raoyang Sag, Bohai Bay Basin, China. *Basin Research*, *32*(1), 116–145.

Chen, S., O'Reilly, S. Y., Zhou, X., Griffin, W. L., Zhang, G., Sun, M., , &(2001). Thermal and petrological structure of the lithosphere beneath Hannuoba, Sino-Korean Craton, China: Evidence from xenoliths. *Lithos*, *56*(4), 267–301.

Cheon, Y., Ha, S., Lee, S., & Son, M. (2020). Tectonic evolution of the Cretaceous Gyeongsang Back-arc Basin, SE Korea: Transition from sinistral transtension to strike-slip kinematics. *Gondwana Research*, *83*, 16–35.

Chinese Academy of Geological Sciences (CAGS). (2002). Geological map of China. Beijing, China: Geological Publishing House Scale 1:5,000,000.

Clinkscales, C., & Kapp, P. (2019). Structural style and kinematics of the Taihang-Luliangshan fold belt, North China: Implications for the Yanshanian orogeny. *Lithosphere*, *11*(6), 767–783.

Clinkscales, C., Kapp, P., & Wang, H. (2020). Exhumation history of the north-central Shanxi Rift, North China, revealed from low-temperature thermochronology. *Earth and Planetary Science Letters*, *536*, 1–14.

Curry, M. A., Barnes, J. B., & Colgan, J. P. (2016). Testing fault growth models with low-temperature thermochronology in the northwest Basin and Range, USA. *Tectonics*, *35*(10), 2467–2492.

Darby, B. J., & Ritts, B. D. (2002). Mesozoic contractional deformation in the middle of the Asian tectonic collage: The intraplate western Ordos fold–thrust belt, China. *Earth and Planetary Science Letters*, *205*(1–2), 13–24.

Davis, G. A., Yadong, Z., Cong, W., Darby, B. J., Changhou, Z., & Gehrels, G. (2001). Mesozoic tectonic evolution of the Yanshan fold and thrust belt, with emphasis on Hebei and Liaoning provinces, northern China. In M. S. Hendrix, & G. A. Davies (Eds.), *Paleozoic and Mesozoic tectonic evolution of central Asia: From continental assembly to intracontinental deformation* (pp. 171–198): Geological Society of America Memoir 194.

de Gelder, G., Fernández-Blanco, D., Melnick, D., Duclaux, G., Bell, R. E., Jara-Muñoz, J., et al. (2019). Lithospheric flexure and rheology determined by climate cycle markers in the Corinth Rift. *Scientific Reports*, *9*(1), 1–12.

Deng, C., Zhu, R., Zhang, R., Ao, H., & Pan, Y. (2008). Timing of the Nihewan formation and faunas. *Quaternary Research*, *69*(1), 77–90.

Donelick, R. A., O'Sullivan, P. B., & Ketcham, R. A. (2005). Apatite fission-track analysis. *Reviews in Mineralogy and Geochemistry*, *58*(1), 49–94.

Duvall, A. R., Clark, M. K., Kirby, E., Farley, K. A., Craddock, W. H., Li, C., & Yuan, D. Y. (2013). Low-temperature thermochronometry along the Kunlun and Haiyuan Faults, NE Tibetan Plateau: Evidence for kinematic change during late-stage orogenesis. *Tectonics*, *32*(5), 1190–1211.

Enkelmann, E., Ratschbacher, L., Jonckheere, R., Nestler, R., Fleischer, M., Gloaguen, R., et al. (2006). Cenozoic exhumation and deformation of northeastern Tibet and the Qinling: Is Tibetan lower crustal flow diverging around the Sichuan Basin? *The Geological Society of America Bulletin*, *118*(5–6), 651–671.

Farley, K. A. (2000). Helium diffusion from apatite: General behavior as illustrated by Durango fluorapatite. *Journal of Geophysical Research*, *105*(B2), 2903–2914. https://doi.org/10.1029/1999JB900348

Farley, K. A. (2002). U-Th/He dating: Techniques, calibrations, and applications. *Reviews in Mineralogy and Geochemistry*, *47*(1), 819–844.

Farley, K. A., Shuster, D. L., & Ketcham, R. A. (2011). U and Th zonation in apatite observed by laser ablation ICPMS, and implications for the (U–Th)/He system. *Geochimica et Cosmochimica Acta*, *75*(16), 4515–4530.

Faulds, J. E., & Varga, R. J. (1998). The role of accommodation zones and transfer zones in the regional segmentation of extended terranes. *Geological Society of America Special Papers*, *323*, 1–45.

Faure, M., Trap, P., Lin, W., Monié, P., & Bruguier, O., 2007, Polyorogenic evolution of the Paleoproterozoic Trans-North China belt, new insights from the Lüliangshan-Hengshan-Wutaishan and Fuping massifs. *Episodes Journal of International Geoscience*, *30*(2), 95–106.

Fitzgerald, P. G., Baldwin, S. L., Webb, L. E., & O'Sullivan, P. B. (2006). Interpretation of (U–Th)/He single grain ages from slowly cooled crustal terranes: A case study from the Transantarctic mountains of southern Victoria Land. *Chemical Geology*, *225*(1–2), 91–120.

Fitzgerald, P. G., & Malusà, M. G. (2019). Concept of the exhumed partial annealing (retention) zone and age-elevation profiles in thermochronology. In M. G. Malusà & P. G. Fitzgerald (Eds.), *Fission-track thermochronology and its application to geology* (pp. 165–189). Cham, Switzerland: Springer. Retrieved from https://link.springer.com/book/10.1007/978-3-319-89421-8#editorsandaffiliations

Flowers, R. M., & Kelley, S. A. (2011). Interpreting data dispersion and "inverted" dates in apatite (U–Th)/He and fission-track datasets: An example from the US midcontinent. *Geochimica et Cosmochimica Acta*, *75*(18), 5169–5186.

Flowers, R. M., Ketcham, R. A., Shuster, D. L., & Farley, K. A. (2009). Apatite (U–Th)/He thermochronometry using a radiation damage accumulation and annealing model. *Geochimica et Cosmochimica Acta*, *73*(8), 2347–2365.

Galbraith, R. F. (2005). *Statistics for fission track analysis*. Boca Raton, FL: Chapman & Hall/CRC Press. Retrieved from https://doi.org/10.1201/9781420034929

Gallagher, K. (2012). Transdimensional inverse thermal history modeling for quantitative thermochronology. *Journal of Geophysical Research*, *117*(B2), B02408. https://doi.org/10.1029/2011JB008825

Gleadow, A. J. W. (1981). Fission-track dating methods: What are the real alternatives? *Nuclear Tracks*, *5*(1–2), 3–14.

Gleadow, A. J. W., Duddy, I. R., Green, P. F., & Hegarty, K. A. (1986). Fission track lengths in the apatite annealing zone and the interpretation of mixed ages. *Earth and Planetary Science Letters*, *78*(2–3), 245–254.

Gleadow, A. J. W., Duddy, I. R., Green, P. F., & Lovering, J. F. (1986). Confined fission track lengths in apatite: A diagnostic tool for thermal history analysis. *Contributions to Mineralogy and Petrology*, *94*(4), 405–415.

Green, P. F. (1988). The relationship between track shortening and fission track age reduction in apatite: Combined influences of inherent instability, annealing anisotropy, length bias and system calibration. *Earth and Planetary Science Letters*, *89*(3–4), 335–352.

Grimmer, J. C., Jonckheere, R., Enkelmann, E., Ratschbacher, L., Hacker, B. R., Blythe, A. E., et al. (2002). Cretaceous−Cenozoic history of the southern Tan-Lu fault zone: Apatite fission-track and structural constraints from the Dabie Shan (eastern China). *Tectonophysics*, *359*(3–4), 225–253.

Guo, P., Niu, Y., Sun, P., Gong, H., & Wang, X. (2020). Lithosphere thickness controls continental basalt compositions: An illustration using Cenozoic basalts from eastern China. *Geology*, *48*(2), 128–133.

He, L. (2014). Numerical modeling of convective erosion and peridotite-melt interaction in big mantle wedge: Implications for the destruction of the North China Craton. *Journal of Geophysical Research: Solid Earth*, *119*(4), 3662–3677. https://doi.org/10.1002/2013JB010657

Hebei Bureau of Geology and Mineral Resources (HBGMR). (1989). Regional geology of Hebei province: Ministry of geology and mineral resources (1, p. 1741): Geological Memoirs. (in Chinese with English summary).

Heberer, B., Anzenbacher, T., Neubauer, F., Genser, J., Dong, Y., & Dunkl, I. (2014). Polyphase exhumation in the western Qinling Mountains, China: Rapid Early Cretaceous cooling along a lithospheric-scale tear fault and pulsed Cenozoic uplift. *Tectonophysics*, *617*, 31–43.

Hellinger, S. J., Shedlock, K. M., Sclater, J. G., & Ye, H. (1985). The Cenozoic evolution of the north China basin. *Tectonics*, *4*(4), 343–358.

Hu, J., Jiang, S. Y., Zhao, H. X., Shao, Y., Zhang, Z. Z., Xiao, E., et al. (2012). Geochemistry and petrogenesis of the Huashan granites and their implications for the Mesozoic tectonic settings in the Xiaoqinling gold mineralization belt, NW China. *Journal of Asian Earth Sciences*, *56*, 276–289.

Hu, S., Raza, A., Min, K., Kohn, B. P., Reiners, P. W., Ketcham, R. A., et al. (2006). Late Mesozoic and Cenozoic thermotectonic evolution along a transect from the north China craton through the Qinling Orogen into the Yangtze craton, central China. *Tectonics*, *25*(6), 1–15.

Hu, Y., Teng, F. Z., Zhang, H. F., Xiao, Y., & Su, B. X. (2016). Metasomatism-induced mantle magnesium isotopic heterogeneity: Evidence from pyroxenites. *Geochimica et Cosmochimica Acta*, *185*, 88–111.

Jolivet, M., De Boisgrollier, T., Petit, C., Fournier, M., Sankov, V. A., Ringenbach, J. C., et al. (2009). How old is the Baikal Rift zone? Insight from apatite fission track thermochronology. *Tectonics*, *28*, 1–21.

Jolivet, M., Ritz, J. F., Vassallo, R., Larroque, C., Braucher, R., Todbileg, M., et al. (2007). Mongolian summits: An uplifted, flat, old but still preserved erosion surface. *Geology*, *35*(10), 871–874.

Ketcham, R. A. (2005). Forward and inverse modeling of low-temperature thermochronometry data. *Reviews in Mineralogy and Geochemistry*, *58*(1), 275–314.

Ketcham, R. A., Carter, A., Donelick, R. A., Barbarand, J., & Hurford, A. J. (2007). Improved modeling of fission-track annealing in apatite. *American Mineralogist*, *92*(5–6), 799–810.

Kröner, A., Wilde, S. A., Li, J. H., & Wang, K. Y. (2005). Age and evolution of a late Archean to Paleoproterozoic upper to lower crustal section in the Wutaishan/Hengshan/Fuping terrain of northern China. *Journal of Asian Earth Sciences*, *24*(5), 577–595.

Kusky, T., Windley, B. F., & Zhai, M. G. (2007). *Tectonic evolution of the north China block: From orogen to craton to orogen* (280, pp. 1–34): Geological Society, London, Special Publications.

Li, J., Zhang, Y., Dong, S., & Johnston, S. T. (2014). Cretaceous tectonic evolution of South China: A preliminary synthesis. *Earth-Science Reviews*, *134*, 98–136.

Li, S., Liu, D., Zhang, Z., & Xu, J. (1988). REE compositional characteristics of Hannuoba basalts. *Chinese Journal of Geochemistry*, *7*(3), 243–251.

Li, S., Zhao, G., Wilde, S. A., Zhang, J., Sun, M., Zhang, G., & Dai, L. (2010). Deformation history of the Hengshan-Wutai-Fuping complexes: Implications for the evolution of the trans–north China orogen. *Gondwana Research*, *18*, 611–631.

Li, S. B., Wang, Y. J., Zhang, Y. Z., Zhang, L. M., Liang, H., & Qiu, W. (2015). Meso-Cenozoic uplifting of South Taihang mountains: Constraints from apatite fission track data. *Geotectonica et Metallogenia*, *39*(3), 460–469.

Li, X., & Song, Y. (2010). Late Cretaceous-Cenozoic exhumation history of the Lüliang mountains, north China craton: Constraint from fission-track thermochronology. *Acta Geologica Sinica-English Edition*, *84*(2), 296–305.

Li, Y., Wu, Q., Pan, J., Zhang, F., & Yu, D. (2013). An upper-mantle S-wave velocity model for East Asia from Rayleigh wave tomography. *Earth and Planetary Science Letters*, *377*, 367–377.

Li, Y., Yang, J., Xia, Z., & Mo, D. (1998). Tectonic geomorphology in the Shanxi graben system, northern China. *Geomorphology*, *23*(1), 77–89.

Lin, W., & Wei, W. (2018). Late Mesozoic extensional tectonics in the north China craton and its adjacent regions: A review and synthesis. *International Geology Review*, *62*, 1–29.

Liu, J., Cai, R., Pearson, D. G., & Scott, J. M. (2019). Thinning and destruction of the lithospheric mantle root beneath the north China craton: A review. *Earth-Science Reviews*, *196*, 1–18.

Liu, J., Zhang, P., Lease, R. O., Zheng, D., Wan, J., Wang, W., & Zhang, H. (2013). Eocene onset and late Miocene acceleration of Cenozoic intracontinental extension in the North Qinling range–Weihe graben: Insights from apatite fission track thermochronology. *Tectonophysics*, *584*, 281–296.

Liu, S., Gurnis, M., Ma, P., & Zhang, B. (2017). Reconstruction of northeast Asian deformation integrated with western Pacific plate subduction since 200 Ma. *Earth-Science Reviews*, *175*, 114–142.

Liu, X., Zhao, D., Li, S., & Wei, W. (2017). Age of the subducting Pacific slab beneath East Asia and its geodynamic implications. *Earth and Planetary Science Letters*, *464*, 166–174.

Lu, H., Wang, X., Wang, X., Chang, X., Zhang, H., Xu, Z., et al. (2019). Formation and evolution of Gobi Desert in central and eastern Asia. *Earth-Science Reviews*, *194*, 251–263.

Meng, X., Ge, M., & Tucker, M. E. (1997). Sequence stratigraphy, sea-level changes and depositional systems in the Cambro-Ordovician of the North China carbonate platform. *Sedimentary Geology*, *114*(1–4), 189–222.

Menzies, M., Xu, Y., Zhang, H., & Fan, W. (2007). Integration of geology, geophysics and geochemistry: A key to understanding the north China craton. *Lithos*, *96*(1–2), 1–21.

Mercier, J. L., Vergely, P., Zhang, Y. Q., Hou, M. J., Bellier, O., & Wang, Y. M. (2013). Structural records of the late Cretaceous–Cenozoic extension in eastern China and the kinematics of the southern tan-Lu and Qinling fault zone (Anhui and Shaanxi provinces, PR China). *Tectonophysics*, *582*, 50–75.

Middleton, T. A., Elliott, J. R., Rhodes, E. J., Sherlock, S., Walker, R. T., Wang, W., et al. (2017). Extension rates across the northern Shanxi Grabens, China, from Quaternary geology, seismicity and geodesy. *Geophysical Journal International*, *209*(2), 535–558.

Middleton, T. A., Walker, R. T., Rood, D. H., Rhodes, E. J., Parsons, B., Lei, Q., et al. (2016). The tectonics of the western Ordos plateau, Ningxia, China: Slip rates on the Luoshan and east Helanshan faults. *Tectonics*, *35*(11), 2754–2777.

Müller, R. D., Zahirovic, S., Williams, S. E., Cannon, J., Seton, M., Bower, D. J., et al. (2019). A global plate model including lithospheric deformation along major rifts and orogens since the Triassic. *Tectonics*, *38*(6), 1884–1907.

Murray, K. E., Orme, D. A., & Reiners, P. W. (2014). Effects of U–Th-rich grain boundary phases on apatite helium ages. *Chemical Geology*, *390*, 135–151.

Nie, J., Song, Y., & King, J. W. (2016). A review of recent advances in red-clay environmental magnetism and paleoclimate history on the Chinese Loess Plateau. *Frontiers of Earth Science*, *4*, 1–13.

Northrup, C. J., Royden, L. H., & Burchfiel, B. C. (1995). Motion of the Pacific plate relative to Eurasia and its potential relation to Cenozoic extension along the eastern margin of Eurasia. *Geology*, *23*(8), 719–722.

Peltzer, G., Tapponnier, P., Zhitao, Z., & Qin, X. Z. (1985). Neogene and Quaternary faulting in and along the Qinling Shan. *Nature*, *317*(6037), 500–505.

Petit, C., & Déverchère, J. (2006). Structure and evolution of the Baikal Rift: A synthesis. *Geochemistry, Geophysics, Geosystems*, *7*(11), 1–26. https://doi.org/10.1029/2006GC001265

Priestley, K., Debayle, E., McKenzie, D., & Pilidou, S. (2006). Upper mantle structure of eastern Asia from multimode surface waveform tomography. *Journal of Geophysical Research*, *111*(B10), B10304. https://doi.org/10.1029/2005JB004082

Pullen, A., Banaszynski, M., Kapp, P., Thomson, S. N., & Cai, F. (2020). A mid-Cretaceous change from fast to slow exhumation of the western Chinese Altai mountains: A climate driven exhumation signal? *Journal of Asian Earth Sciences*, *197*, 1–12.

Qi, J., & Yang, Q. (2010). Cenozoic structural deformation and dynamic processes of the Bohai Bay basin province, China. *Marine and Petroleum Geology*, *27*(4), 757–771.

Qing, J. C., Ji, J. Q., Wang, J. D., Peng, Q. L., Niu, X. L., & Ge, Z. H. (2008). Apatite fission track study of Cenozoic uplifting and exhumation of Wutai Mountain, China. *Chinese Journal of Geophysics*, *51*(2), 256–264.

Qiu, N., Zuo, Y., Zhou, X., & Li, C. (2010). Geothermal regime of the Bohai offshore area, Bohai Bay basin, north China. *Energy Exploration & Exploitation*, *28*(5), 327–350.

Qu, W., Lu, Z., Zhang, Q., Wang, Q., Hao, M., Zhu, W., & Qu, F. (2018). Crustal deformation and strain fields of the Weihe Basin and surrounding area of central China based on GPS observations and kinematic models. *Journal of Geodynamics*, *120*, 1–10.

Ratschbacher, L., Hacker, B. R., Calvert, A., Webb, L. E., Grimmer, J. C., McWilliams, M. O., et al. (2003). Tectonics of the Qinling (Central China): Tectonostratigraphy, geochronology, and deformation history. *Tectonophysics*, *366*(1–2), 1–53.

Ratschbacher, L., Hacker, B. R., Webb, L. E., McWilliams, M., Ireland, T., Dong, S., et al. (2000). Exhumation of the ultrahigh-pressure continental crust in east central China: Cretaceous and Cenozoic unroofing and the Tan-Lu fault. *Journal of Geophysical Research*, *105*(B6), 13303–13338. https://doi.org/10.1029/2000JB900040

Reiners, P. W., & Brandon, M. T. (2006). Using thermochronology to understand orogenic erosion. *Annual Review of Earth and Planetary Sciences*, *34*, 419–466.

Richardson, N. J., Densmore, A. L., Seward, D., Fowler, A., Wipf, M., Ellis, M. A., et al. (2008). Extraordinary denudation in the Sichuan Basin: Insights from low-temperature thermochronology adjacent to the eastern margin of the Tibetan Plateau. *Journal of Geophysical Research*, *113*(B4), B04409. https://doi.org/10.1029/2006JB004739

Ritts, B. D., Weislogel, A., Graham, S. A., & Darby, B. J. (2009). Mesozoic tectonics and sedimentation of the Giant polyphase nonmarine intraplate Ordos Basin. *Western North China Block: International Geology Review*, *51*(2), 95–115.

Ryan, W. B., Carbotte, S. M., Coplan, J. O., O'Hara, S., Melkonian, A., Arko, R., et al. (2009). Global multi-resolution topography synthesis. *Geochemistry, Geophysics, Geosystems*, *10*(3), Q03014. https://doi.org/10.1029/2008GC002332

SBGMR, (Shanxi Bureau of Geology and Mineral Resources). (1989). *Regional geology of Shanxi Province* (p. 780). Beijing, China: Geological Publishing House.

Seton, M., Flament, N., Whittaker, J., Müller, R. D., Gurnis, M., & Bower, D. J. (2015). Ridge subduction sparked reorganization of the Pacific plate-mantle system 60–50 million years ago. *Geophysical Research Letters*, *42*(6), 1732–1740. https://doi.org/10.1002/2015GL063057

Shi, W., Cen, M., Chen, L., Wang, Y., Chen, X., Li, J., & Chen, P. (2015). Evolution of the late Cenozoic tectonic stress regime in the Shanxi Rift, central North China Plate inferred from new fault kinematic analysis. *Journal of Asian Earth Sciences*, *114*, 54–72.

Shi, W., Chen, L., Chen, X., Cen, M., & Zhang, Y. (2019). The Cenozoic tectonic evolution of the faulted basins in the northern margin of the Eastern Qinling Mountains, Central China: Constraints from fault kinematic analysis. *Journal of Asian Earth Sciences*, *173*, 204–224.

Shi, W., Dong, S., & Hu, J. (2020). Neotectonics around the Ordos block, north China: A review and new insights. *Earth-Science Reviews*, *200*, 1–34.

Shuster, D. L., Flowers, R. M., & Farley, K. A. (2006). The influence of natural radiation damage on helium diffusion kinetics in apatite. *Earth and Planetary Science Letters*, *249*(3–4), 148–161.

Stein, R. S., King, G. C., & Rundle, J. B. (1988). The growth of geological structures by repeated earthquakes 2. Field examples of continental dip-slip faults. *Journal of Geophysical Research*, *93*(B11), 13319–13331.

Styron, R., Taylor, M., & Okoronkwo, K. (2010). Database of active structures from the Indo-Asian collision. *Eos, Transactions American Geophysical Union*, *91*(20), 181–182.

Tang, Y. J., Zhang, H. F., & Ying, J. F. (2006). Asthenosphere–lithospheric mantle interaction in an extensional regime: Implication from the geochemistry of Cenozoic basalts from Taihang mountains, north China craton. *Chemical Geology*, *233*(3–4), 309–327.

Tapponnier, P., & Molnar, P. (1977). Active faulting and tectonics in China. *Journal of Geophysical Research*, *82*(20), 2905–2930.

Taylor, M., & Yin, A. (2009). Active structures of the Himalayan-Tibetan orogen and their relationships to earthquake distribution, contemporary strain field, and Cenozoic volcanism. *Geosphere*, *5*(3), 199–214.

Tian, X., Zelt, C. A., Wang, F., Jia, S., & Liu, Q. (2014). Crust structure of the North China Craton from a long-range seismic wide-angle-reflection/refraction data. *Tectonophysics*, *634*, 237–245.

Trap, P., Faure, M., Lin, W., & Meffre, S. (2009). *The Lüliang Massif: A Key Area for the Understanding of the Palaeoproterozoic Trans-North China belt, north China craton* (323, pp. 99–125): Geological Society, London, Special Publications.

Trap, P., Faure, M., Lin, W., & Monié, P. (2007). Late Paleoproterozoic (1900–1800 Ma) nappe stacking and polyphase deformation in the Hengshan–Wutaishan area: Implications for the understanding of the Trans-North-China belt, north China craton. *Precambrian Research*, *156*(1–2), 85–106.

Vermeesch, P., Seward, D., Latkoczy, C., Wipf, M., Günther, D., & Baur, H. (2007). α-Emitting mineral inclusions in apatite, their effect on (U–Th)/He ages, and how to reduce it. *Geochimica et Cosmochimica Acta*, *71*(7), 1737–1746.

Wang, J. M. (1987). The Fenwei rift and its recent periodic activity. *Tectonophysics*, *133*(3–4), 257–275.

Wang, Q., Li, C., Tian, G., Zhang, W., Liu, C., Ning, L., et al. (2002). Tremendous change of the earth surface system and tectonic setting of salt-lake formation in Yuncheng Basin since 7.1 Ma. *Science in China-Series D: Earth Sciences*, *45*(2), 110–122.

Wang, Y.-T., Ye, H.-S., Ye, A.-W., Liu, S.-L., Hao, J.-L., Liu, J.-C., et al. (2019). Cooling and uplift history of the Niangniangshan granitic pluton in the Xiaoqinling goldfield, central China: Implications for tectonic evolution and gold mineralization. *Geological Journal*, *55*, 1–11.

Webb, A. A. G. (2007). *Contractional and extensional tectonics during the India-Asia collision* (Ph.D. thesis). Los Angeles, CA: University of California.

Wolf, R. A., Farley, K. A., & Kass, D. M. (1998). Modeling of the temperature sensitivity of the apatite (U–Th)/He thermochronometer. *Chemical Geology*, *148*(1–2), 105–114.

Wu, J. T., & Wu, J. (2019). Izanagi-Pacific ridge subduction revealed by a 56 to 46 Ma magmatic gap along the northeast Asian margin. *Geology*, *47*(10), 953–957.

Xia, B., Thybo, H., & Artemieva, I. M. (2017). Seismic crustal structure of the North China Craton and surrounding area: Synthesis and analysis. *Journal of Geophysical Research: Solid Earth*, *122*(7), 5181–5207. https://doi.org/10.1002/2016JB013848

Xiao, X. M., Zhao, B. Q., Thu, Z. L., Song, Z. G., & Wilkins, R. W. T. (2005). Upper Paleozoic petroleum system, Ordos Basin, China. *Marine and Petroleum Geology*, *22*(8), 945–963.

Xiong, J., Li, Y., Zheng, W., Zhang, P., Lei, J., Zhong, Y., et al. (2018). Climatically driven formation of the Tangxian planation surface in north China: An example from northwestern Zhongtiao Shan of the Shanxi graben system. *Lithosphere*, *10*(4), 530–544.

Xiong, J., Li, Y., Zhong, Y., Si, S., Lei, J., Xin, W., et al. (2017). Paleomagnetic age of the Tangxian planation surface, northwestern Zhongtiao Shan of the Shanxi graben system, north China. *Geomorphology*, *283*, 17–31.

Xu, H., Liu, Y., Kuang, H., & Peng, N. (2019). Late Jurassic fluvial–eolian deposits from the Tianchihe formation, Ningwu–Jingle basin, Shanxi province, China. *Journal of Asian Earth Sciences*, *174*, 245–262.

Xu, X., & Ma, X. (1992). Geodynamics of the Shanxi rift system, China. *Tectonophysics*, *208*(1–3), 325–340.

Xu, X., Ma, X., & Deng, Q. (1993). Neotectonic activity along the Shanxi rift system, China. *Tectonophysics*, *219*(4), 305–325.

Xu, Y., He, H., Deng, Q., Allen, M. B., Sun, H., & Bi, L. (2018). The CE 1303 Hongdong earthquake and the Huoshan Piedmont fault, Shanxi graben: Implications for magnitude limits of normal fault earthquakes. *Journal of Geophysical Research: Solid Earth*, *123*(4), 3098–3121. https://doi.org/10.1002/2017JB014928

Xu, Y. G. (2007). Diachronous lithospheric thinning of the North China Craton and formation of the Daxin'anling–Taihangshan gravity lineament. *Lithos*, *96*(1–2), 281–298.

Yang, J. H., Wu, F. Y., Chung, S. L., Lo, C. H., Wilde, S. A., & Davis, G. A. (2007). Rapid exhumation and cooling of the Liaonan metamorphic core complex: Inferences from $^{40}Ar/^{39}Ar$ thermochronology and implications for Late Mesozoic extension in the eastern North China Craton. *The Geological Society of America Bulletin*, *119*(11–12), 1405–1414.

Yang, Z., Shen, C., Ratschbacher, L., Enkelmann, E., Jonckheere, R., Wauschkuhn, B., & Dong, Y. (2017). Sichuan basin and beyond: Eastward foreland growth of the Tibetan plateau from an integration of late Cretaceous-Cenozoic fission track and (U-Th)/He ages of the eastern Tibetan plateau, Qinling, and Daba Shan. *Journal of Geophysical Research: Solid Earth*, *122*(6), 4712–4740. https://doi.org/10.1002/2016JB013751

Yin, A. (2000). Mode of Cenozoic east-west extension in Tibet suggesting a common origin of rifts in Asia during the Indo-Asian collision. *Journal of Geophysical Research*, *105*(B9), 21745–21759.

Yin, A. (2010). Cenozoic tectonic evolution of Asia: A preliminary synthesis. *Tectonophysics*, *488*(1–4), 293–325.

Yu, F., & Koyi, H. (2016). Cenozoic tectonic model of the Bohai Bay basin in China. *Geological Magazine*, *153*(5–6), 866–886.

Yu, X., Liu, J., Li, C., Chen, S., & Dai, Y. (2013). Zircon U–Pb dating and Hf isotope analysis on the Taihua complex: Constraints on the formation and evolution of the Trans-North China orogen. *Precambrian Research*, *230*, 31–44.

Yu, X., Liu, J., Zhang, D., Zheng, Y., Li, C., Chen, S., & Li, T. (2013). Uprising period and elevation of the Wenyu granitic pluton in the Xiaoqinling District, Central China. *Chinese Science Bulletin*, *58*(35), 4459–4471.

Zhang, A., Yang, Z., Zhong, J., & Mi, F. (1995). Characteristics of late Quaternary activity along the southern border fault zone of Weihe graben basin. *Quaternary International*, *25*, 25–31.

Zhang, J., Qu, J., Zhang, B., Zhao, H., Niu, P., Zhao, S., et al. (2020). Mesozoic intraplate deformation of the central North China Craton: Mechanism and tectonic setting. *Journal of Asian Earth Sciences*, *192*, 1–29.

Zhang, J., & Zheng, Y. (1999). Multistage extension and age dating of the Xiaoqinling metamorphic core complex, central China. *Acta Geologica Sinica-English Edition*, *73*(2), 139–147.

Zhang, J. S., Xu, J., Wan, J. L., Zhang, J. X., & Gao, Z. W. (2002). Meso-Cenozoic detachment zones in the front of the Taihang Mountains and their fission-track ages. *Geological Bulletin of China*, *21*(4–5), 207–210.

Zhang, K. (2008). Planation surfaces in China: One hundred years of investigation. *Geological Society, London, Special Publications*, *301*(1), 171–178.

Zhang, S. H., Zhao, Y., Davis, G. A., Ye, H., & Wu, F. (2014). Temporal and spatial variations of Mesozoic magmatism and deformation in the North China Craton: Implications for lithospheric thinning and decratonization. *Earth-Science Reviews*, *131*, 49–87. https://doi.org/10.1016/j.earscirev.2013.12.004

Zhang, Y., Dong, S., Zhao, Y., & Zhang, T. (2008). Jurassic tectonics of North China: A synthetic view. *Acta Geologica Sinica-English Edition*, *82*(2), 310–326.

Zhang, Y., Ma, Y., Nong, Y., Shi, W., & Shuwen, D. (2003). Cenozoic extensional stress evolution in North China. *Journal of Geodynamics*, *36*(5), 591–613.

Zhang, Y., Vergèly, P., Mercier, J. L., Yongmin, W., Yong, Z., & Dezhi, H. (1999). Kinematic history and changes in the tectonic stress regime during the Cenozoic along the Qinling and southern Tanlu fault zones. *Acta Geologica Sinica-English Edition*, *73*(3), 264–274.

10.1029/2020TC006416

Zhang, Y. Q., Mercier, J. L., & Vergély, P. (1998). Extension in the graben systems around the Ordos (China), and its contribution to the extrusion tectonics of south China with respect to Gobi-Mongolia. *Tectonophysics*, *285*(1–2), 41–75.

Zhang, Z., Teng, J., Romanelli, F., Braitenberg, C., Ding, Z., Zhang, X., et al. (2014). Geophysical constrains on the link between cratonization and orogeny: Evidence from the Tibetan Plateau and the north China craton. *Earth-Science Reviews*, *130*, 1–48. https://doi.org/10.1016/j.earscirev.2013.12.005

Zhao, H., Zhang, J., Qu, J., Zhang, B., Yun, L., Li, J., , &(2020). Nature of the eastern boundary of the Mesozoic Ordos Basin and the formation of the Lüliangshan anticline. *The Journal of Geology*, *128*(2), 157–187.

Zhao, J., Liu, C., Mountney, N., Lu, J., Cao, J., Yang, Y., & Xue, R. (2016). Timing of uplift and evolution of the Lüliang mountains, north China craton. *Science China Earth Sciences*, *59*(1), 58–69.